Specific Surface Area and Bulk Strain: Important Material Metrics Determining the Electrochemical Performance of Li- and Mn-Rich Layered Oxides

Benjamin Strehle,*,z Jiyoung Yoon, Franziska Friedrich, and Hubert A. Gasteiger**

Chair of Technical Electrochemistry, Department of Chemistry and Catalysis Research Center, Technical University of Munich, D-85748 Garching, Germany

Li- and Mn-rich layered oxides are a promising next-generation cathode active material (CAM) for automotive applications. Beyond well-known challenges such as voltage fading and oxygen release, their commercialization also depends on practical considerations including cost and energy density. While the cost requirement for these materials could be satisfied by eliminating cobalt, the volumetric energy density requirement might imply the transition from the most widely used porous structure to a more densely packed structure. Here, we investigated five Li- and Mn-rich layered oxides which were synthesized by various routes to obtain CAMs with different morphologies (porous vs dense), transition-metal compositions (Co-containing vs Co-free), and agglomerates sizes ($\approx 6-12$ μm). The as-received materials were characterized, e.g., by gas physisorption, Hg intrusion porosimetry, as well as X-ray powder diffraction, and were electrochemically tested by a discharge rate test. Thus, we identified two important material metrics which determine the initial electrochemical performance of Li- and Mn-rich CAMs, and which might be used as performance predictors: (i) the surface area in contact with the electrolyte that defines the effective current density which is applied to the surface of the CAMs, and (ii) the microstrain in the bulk that affects distinct redox features during cycling. © 2022 The Author(s). Published on behalf of The Electrochemical Society by IOP Publishing Limited. This is an open access article distributed under the terms of the Creative Commons Attribution 4.0 License (CC BY, http://creativecommons.org/licenses/by/4.0/), which permits unrestricted reuse of the work in any medium, provided the original work is properly cited. [DOI: 10.1149/1945-7111/ac766c]

Li- and Mn-rich layered oxides are considered as potential next-generation cathode active material (CAM) for automotive applications.[1–3] They offer exceptionally high specific capacities of about 250 mAh g^{-1} in combination with very low material cost.[4,5] The capacity increase in the over-lithiated compared to stoichiometric CAMs originates from a slight rearrangement of the layered structure, Li[Li$_\delta$TM$_{1-\delta}$]O$_2$.[5,6] While stoichiometric CAMs such as NCMs (Li[Ni$_{1-x-y}$Co$_x$Mn$_y$]O$_2$) and NCAs (Li[Ni$_{1-x-y}$Co$_x$Al$_y$]O$_2$) are barely over-lithiated, with δ being close to zero, Li- and Mn-rich CAMs possess δ values between 0.1 and 0.2. Apart from Mn, the transition-metal (TM) mixture typically contains minor fractions of Ni and Co, but Co-free variants are also reported in the literature.[7–10] Omitting Co is important to reducing the cost, since it is the most expensive element among the three transition-metals and it is further problematic due to sustainability and geopolitical aspects.[11–13] The practical application of Li- and Mn-rich CAMs is hindered by several significant challenges,[4,14] including a pronounced voltage hysteresis within a charge-discharge cycle,[15,16] discharge voltage fading during long-term cycling,[10,17] and oxygen release within the first cycles,[18,19] which leads to both surface reconstruction[20] and electrolyte decomposition.[21] All of these problems are well-known, and numerous mitigation strategies are suggested in the literature.[5,22,23] However, implications originating from the morphology of the CAMs have gotten little attention yet.

A recent study from our university systematically compared the pilot scale production process of $\approx 6-7$ Ah multi-layer pouch cells using either a Ni-rich CAM (NCA with 81% Ni) or a Li- and Mn-rich CAM.[24,25] Here, the latter could not be calendered to commonly used electrode porosities of $\approx 30\%$. The authors attributed this issue to the morphology of the Li- and Mn-rich CAM, which has a significant fraction of internal porosity within the secondary agglomerates. This internal porosity cannot be removed by calendering, because severe defects such as the embossing of the aluminum current collector foil set in before the breakage of the CAM particles, thereby preventing calendering on an automated production line below a porosity of $\approx 42\%$. At such a high porosity,

the resulting electrode density was only ≈ 2.3 g$_{electrode}$ cm^{-3}$_{electrode}$, $\approx 15\%$ lower than the initially targeted electrode density of ≈ 2.7 g$_{electrode}$ cm^{-3}$_{electrode}$ (for $\approx 32\%$ porosity),[24] on which projections on the potential energy density of Li- and Mn-rich cathodes are typically based on.[14] This issue is addressed in the review articles by Zheng et al.[14] and Hy et al.[22] in view of the low tap density of Li- and Mn-rich CAM powders (typically $\leqslant 2$ g cm^{-3}). The extent of internal porosity further finds expression in the specific surface area of the pristine CAMs, which is usually on the order of ≈ 5 m^2 g^{-1} for over-lithiated oxides, but < 1 m^2 g^{-1} for stoichiometric oxides.[21] Therefore, we conclude that most of the Li- and Mn-rich CAMs investigated in the literature feature a high internal porosity. This calls for improved or alternative synthesis routes in order to obtain more densely packed CAMs and to increase their volumetric energy density.[14,22]

Another property which will be addressed in this work is the strain in cathode active materials, or more precisely, the microstrain on an atomic level. Microstrain has its origin in crystal defects, which can be classified either as point defects (e.g., local displacements,[26] vacancies,[27] and site disorder[28]), line defects (e.g., dislocations[29]), planar defects (e.g., stacking faults[30] and twin boundaries[31]) or volume defects (e.g., voids[32]). All these defects cause a residual stress in the material that is otherwise in equilibrium with its surrounding, i.e., it does not experience any external forces or temperature gradient.[33] Consequently, the residual tensile and compressive forces have to be balanced inside the material. In this context, microstrain represents the normalized displacement of atoms from their ideal position within the lattice, especially in the vicinity of the defect site due to the acting forces. This distortion leads to line broadening in the diffraction profile of the sample and can be quantified by a size/strain analysis, e.g., with the Williamson-Hall method.[34–36] Here, size broadening (as known from the Scherrer equation) originates from extended imperfections, which split a crystal into smaller incoherently diffracting domains. Microstrain arises from more localized defects, but the differentiation between both contributions is sometimes difficult.[37] Mathematically, both scale solely with the diffraction angle θ and they can be separated according to their different θ-dependence. At high SOCs, however, the reflections of layered oxides typically vary non-monotonically with θ due to an additional *hkl* dependence. During the refinement, this anisotropic line broadening can be modeled by the phenomenological model from Stephens.[38–40] It is believed to be caused, e.g., by the

*Electrochemical Society Student Member.
**Electrochemical Society Fellow.
zE-mail: benjamin.strehle@tum.de

statistical distribution of stacking faults in layered oxides,[41] oxygen-deficient regions,[42] or a density variation of lithium atoms (either from grain to grain or even within a grain).[43] For LNO ($LiNiO_2$), the occurrence of anisotropic strain broadening and stacking faults upon delithiation could be recently monitored by operando X-ray powder diffraction (XPD).[30] Furthermore, microstrain effects are discussed as important nucleation sites for intra-granular cracking.[44]

In the present study, we investigated five Li- and Mn-rich layered oxides, which all have the same degree of over-lithiation, but which were subjected to different synthesis conditions by our cooperation partner BASF SE. Depending on the used proprietary synthesis routes, the five CAMs can be differentiated into three categories in terms of: (i) morphology, differentiating porous from dense CAMs; (ii) transition-metal composition, differentiating Co-containing from Co-free CAMs; and, (iii) secondary agglomerate size, ranging from D_{50} values of ≈ 6 to ≈ 12 μm, respectively. We characterized the as-received materials by a series of techniques, namely scanning electron microscopy, particle size analysis by laser scattering, gas physisorption, Hg intrusion porosimetry, and X-ray powder diffraction, which all target at their initial material metrics. These metrics are related to important surface and bulk properties of the CAMs, which will be then correlated in a quantitative manner to their initial electrochemical performance during a discharge rate test.

Experimental

Materials.—We investigated five Li- and Mn-rich layered oxides provided by BASF SE (Germany), which differ with respect to their morphology, transition-metal (TM) composition, and particle size. The degree of over-lithiation is similar among the five CAMs and amounts to $\delta = 0.14 \pm 0.01$ in $Li[Li_\delta TM_{1-\delta}]O_2$, which can be also written as 0.33 $Li_2MnO_3 \cdot (1-x)$ $LiTMO_2$" notation used by Teufl et al.[20] Throughout this work, the CAMs are abbreviated according to the "morphology-cobalt content-particle size" nomenclature serving as a CAM ID. This specifies the morphology of the secondary agglomerates as either porous (P) or dense (D), achieved by two different proprietary synthesis routes, the cobalt content as either Co-containing (wCo) or Co-free (woCo), as well as the particle size, referring to the targeted diameter of the secondary agglomerates (in μm). Consequently, the five investigated CAMs are referred to as P-wCo-10, D-wCo-10, D-wCo-6, P-woCo-6, and D-woCo-6.

In order to modify the surface (specific surface area) and bulk properties (microstrain), we further subjected the as-received D-woCo-6 CAM to a post-calcination step. Here, ≈ 4 g of the CAM powder were weighed into an alumina crucible (GTS Keramik, Germany) and heat-treated in a tube furnace (Carbolite, Germany) for 5 h at 1000 °C (prior heating at 10 °C min^{-1} and subsequent cooling at 2 °C min^{-1}) in an inert argon atmosphere (99.999% purity, Westfalen, Germany; flow rate of ≈ 1 l min^{-1}). The post-calcination temperature of 1000 °C intentionally goes beyond the original sintering temperature of ≈ 930 °C for the as-received CAM. Afterwards, the post-calcined sample was handled and analyzed just like the other CAMs, and it is referred to as D-woCo-6-1000C in the following.

Scanning electron microscopy (SEM).—The morphology of the CAMs was evaluated by scanning electron microscopy (JSM-7500F, JEOL, Japan) in backscattering mode at an accelerating voltage of 1 kV. We measured both top-view images of the pristine CAM powders and cross-sectional images of the pristine, compressed electrodes. The cross-sections were either prepared by mechanical polishing, following the procedure described by Friedrich et al. (i.e., the samples were embedded into epoxy resin and in the final step polished with a 0.05 μm Al_2O_3 suspension),[40] or by focused argon-ion beam (FIB) milling with a JEOL cross-section polisher (IB-19530CP, JEOL, Japan). In the latter case, the electrodes were first cut with a razor blade to create a clean cutting edge; subsequently, the electrodes were milled along this edge at a

temperature of −100 °C, and in the final step with an acceleration voltage of 4 kV for 1.5–3 h (argon-ion beam alternatingly on/off for 10/10 s).

Particle size analysis.—The volumetric particle size distribution of the CAMs was measured by dynamic laser scattering (DLS; HORIBA LA-960, Retsch Technology, Germany), which is based on the Mie scattering theory. One tip of a spatula of the pristine CAM powder was dispersed in ethanol by sonication and then analyzed in a flow-through cell. The measurement was evaluated with a real part refractive index of 2.11 for the CAM (assuming MnO as reference material[45]) and of 1.36 for ethanol. We report the D_{50} values of the different CAMs.

Gas physisorption analysis.—The specific surface area of the CAMs was determined by gas physisorption (Autosorb-iQ, Quantachrome, USA) at 77 K using nitrogen as adsorbate. Beforehand, the pristine CAM powders were outgassed at 120 °C for 12 h under dynamic vacuum. The sample mass was chosen to achieve an absolute surface area of 2.5–5.0 m^2 inside the sample holder. Adsorption isotherms were measured with 11 data points in the relative pressure range of $0.05 \leqslant p/p_0 \leqslant 0.30$ (p/p_0 tolerance of −0.003 and +0.009, equilibration time of 3 min). The specific surface area was calculated according to the Brunauer-Emmet-Teller (BET) theory, whereby the ideal linear range is selected by the Micropore BET Assistant of the ASiQwin software (typically 7 out of the 11 points).[46]

Mercury intrusion porosimetry (MIP).—The pore size distribution and pore volume of the CAMs were measured with a Micromeritics AutoPore V instrument (Micromeritics, USA). The as-received CAM powders were dried overnight at 120 °C under dynamic vacuum and then loaded into the penetrometer (sample holder) with a bulb and stem volume of 3.00 and 0.412 cm^3, respectively. The sample mass was between 0.5−1.0 g, targeting at an usage of $\approx 60\%$ of the stem volume filled with mercury. The penetrometer was filled at a pressure of 0.007 MPa. First, the low-pressure port measures the mercury intrusion up to a pressure of 0.35 MPa (one data point every 0.014 MPa, equilibration time of 10 s), while the subsequent high-pressure port goes all the way up to 410 MPa (>30 points per decade, equilibration rate of 5 μl $(g \cdot s)^{-1}$). The pore diameter (d_{pore}) is calculated with the Washburn equation:

$$d_{pore} = -\frac{4 \cdot \gamma_{Hg} \cdot \cos \theta_{Hg}}{p} \quad [1]$$

where γ_{Hg} is the surface tension of Hg (0.485 N m^{-1} at 20 °C), θ_{Hg} is the contact angle of Hg (130°), and p is the applied pressure. Consequently, the measurable pore diameter ranges from ≈ 180 μm to ≈ 3 nm.

The intruded mercury volume was corrected with a blank run of the empty penetrometer (filled only with Hg). Since the correction might not be perfect at the high-pressure end (e.g., due to heating of the hydraulic oil), we further omitted negative intrusion values (typically $\leqslant 5$ mm^3 g^{-1} at $\leqslant 20$ nm). Following our previous study,[24] we assigned the pore volume obtained for pore diameters smaller than 300 nm to that of intra-particular pores ($v_{pore,intra}$) inside the secondary agglomerates. The associated intra-particular porosity (ε_{intra}) was calculated as follows:

$$\varepsilon_{intra} = \frac{v_{pore,intra}}{v_{pore,intra} + \frac{1}{\rho_{cryst}}} \quad [2]$$

where ρ_{cryst} is the crystallographic density of the layered oxides (≈ 4.35 g cm^{-3}).

X-ray powder diffraction (XPD).—The pristine CAM powders were loaded into 0.3 mm borosilicate capillaries and measured in the

2θ range of 5°–60° (one data point every 0.015°) for $\approx$14 h at our in-house STOE STADI P diffractometer (STOE, Germany). This instrument works in transmission mode using Mo-K$_{\alpha 1}$ radiation (λ = 0.7093 Å), a Ge(111) monochromator, and a Mythen 1K detector. The XPD data were analyzed with the Topas software package.[47] The layered oxides were treated with the structure-independent Le Bail method using the $C2/m$ symmetry (space group no. 12).[48] In contrast to the Rietveld method, this approach does not require the exact composition of the CAMs or any sophisticated structural model. While the Rietveld method primarily targets at extracting crystallographic information (e.g., atomic positions and site occupancy factors) by modelling the reflection intensity, the here applied Le Bail method focuses on the line broadening in order to obtain real structure information (i.e., crystallite size and microstrain).

We refined the background (Chebyshev polynomial with 12 coefficients), instrumental parameters (zero shift and axial divergence), the four lattice parameters (a, b, c, and β) as well as the intensity of each individual reflection (according to the Le Bail method). However, we were particularly interested in the line broadening of the reflections (Γ_{hkl}):

$$\Gamma_{hkl} = \Gamma_{instrument} + \Gamma_{size} + \Gamma_{strain} \quad [3]$$

which has contributions from the instrument ($\Gamma_{instrument}$) and from the sample (Γ_{size} and Γ_{strain}). The instrumental broadening was determined with a standard silicon material using the Thompson-Cox-Hastings pseudo-Voigt function (Topas command *TCHZ_Peak_Type*, parameters U, W, and X activated).[37] The crystallite size of the sample leads to line broadening according to the well-known Scherrer equation:

$$\Gamma_{size} = \frac{K \cdot \lambda}{L_{vol} \cdot \cos\theta} \quad [4]$$

where K is a shape factor (on the order of 1), λ is the wavelength, θ is the Bragg angle, and L_{vol} is the volume-weighted mean column length of the crystallites. Assuming spherical crystallites, their average diameter corresponds to $d_{sphere} = 4/3 \cdot L_{vol}$.[37] Note that the Scherrer equation is only applicable to sub-μm crystallites (L_{vol} less than $\approx$200 nm). Finally, there is a microstrain contribution of the sample:

$$\Gamma_{strain} = 4 \cdot \varepsilon_0 \cdot \tan\theta \quad [5]$$

where $\varepsilon_0 = \Delta d/d$ is the mean lattice spacing deviation. This lattice imperfection is caused by the displacement of atoms from their ideal position, e.g., due to point defects such as vacancies and interstitials.

The two contributions of the sample broadening can be separated by their θ-dependence, $\Gamma_{size} \propto 1/\cos\theta$ vs $\Gamma_{strain} \propto \tan\theta$. Another important aspect of the size/strain analysis addresses the calculation method of the line broadening. The Topas Technical Reference recommends extracting L_{vol} from the integral breadth-based $\Gamma_{size(IB)}$, while ε_0 should rely on the full width at half maximum-based $\Gamma_{strain(FWHM)}$.[37] The integral breadth of a reflection is obtained from dividing the line profile area by its height, and the crystallite size determined therefrom is fairly independent of the size distribution and shape (with K set to 1). Following this advice, we used the *LVol_FWHM_CS_G_L* and *e0_from_Strain* commands in Topas, which both comprise Lorentzian and Gaussian component convolutions. Thus, there are a total of four parameters to describe the line profile of the layered oxide, but we deactivated the parameters with a limit warning from the program (individually for each CAM). This could happen when the crystallite size is too large or the microstrain is too small to be quantifiable, which might apply only to one component (Lorentzian or Gaussian) or to the entire contribution (size or strain). Please note that the applied commands describe an isotropic line broadening, i.e., the width of the reflections scales solely with 2θ, but there is no anisotropic dependence on hkl. Furthermore, we did not implement an additional broadening of the

superstructure reflections, because they barely affect the size/strain values extracted from the entire diffractogram.

During the review process, it was pointed out that silicon is not the best choice for calibrating the instrumental broadening of the diffractometer, as it might contribute sample-related broadening effects. Therefore, we recommend LaB$_6$ or Na$_2$Ca$_3$Al$_2$F$_{14}$ (NAC) as line profile standards in future studies. Assuming that the measured broadening originates solely from the CAMs, the size/strain analysis would yield a maximum deviation of 0.02% (absolute) higher microstrain values; however, the observed trend between the CAMs is unaffected.

Electrochemical characterization.—Cathode coatings consist of the CAM powder, conductive carbon (Super C65, Timcal, Switzerland), and polyvinylidene fluoride binder (PVDF, Kynar HSV 900, Arkema, France) at a weight ratio of 90:5:5 (for the Co-containing CAMs) or 92.5:4.0:3.5 (for the Co-free CAMs). The slurry was prepared with N-methyl-2-pyrrolidone (NMP, anhydrous, 99.5%, Sigma-Aldrich, Germany) in several steps in a planetary orbital mixer (Thinky, USA) and then cast onto the 15 μm thick aluminum current collector foil (MTI, USA). After drying at 50 °C in a convection oven, the loading of the cathode sheets amounts to $\approx$5.0–6.0 mg$_{CAM}$ cm^{-2} (for the Co-containing CAMs) and $\approx$6.5–7.0 mg$_{CAM}$ cm^{-2} (for the Co-free CAMs); the CAM loading of each electrode was determined with a precision of ±0.05 mg$_{CAM}$ cm^{-2}. Disk-shaped electrodes with a diameter of 10 mm were punched out of the cathode sheets and compressed at 2 t for 20 s. The electrodes were dried overnight at 120 °C in a vacuum oven (Büchi, Switzerland) and then inertly transferred into an argon-filled glove box (<0.1 ppm O$_2$ and H$_2$O, MBraun, Germany).

Electrochemical testing was conducted in 3-electrode Swagelok® T-cells with a lithium metal counter-electrode (Li-CE, with Ø 11 mm of a 450 μm thick lithium foil, Albemarle, USA) and a lithium metal reference-electrode (Li-RE, with Ø 6 mm). Anode and cathode were separated by two glass-fiber separators (Ø 11 mm, glass microfiber filter 691, VWR, Germany), which were soaked with 60 μl of LP57 electrolyte (1M LiPF$_6$ in EC:EMC = 3:7 by weight, BASF SE, Germany). The cells were measured at 25 °C in a temperature-controlled chamber (Binder, Germany) with a battery cycler (Series 4000, Maccor, USA).

The cathode potential was controlled vs the Li-RE and the C-rate was based on a nominal capacity of 250 mAh g^{-1} (i.e., 1C $\equiv$ 250 mA g^{-1}). The cycling protocol started with an activation cycle in the potential window of 2.0–4.8 V vs Li$^+$/Li at a C-rate of C/15 or C/10, whereby the latter was completed with a constant voltage (CV) hold at 4.8 V for 1 h. Following two subsequent stabilization cycles between 2.0–4.7 V vs Li$^+$/Li at C/10 (without CV hold), the cells passed a discharge rate test going in nine steps from 10C to C/50 for 2 cycles each. The potential window was fixed between 2.0−4.7 V vs Li$^+$/Li and the discharge was done consecutively at 10C, 5C, 2C, 1C, C/2, C/5, C/10, C/20, and C/50, respectively. The charge had a C-rate of less or equal than C/2, i.e., the charge was limited to C/2 when the discharge was faster, but both were equal at slower rates. Furthermore, each charge step was completed by a CV hold at 4.7 V vs Li$^+$/Li until the current dropped below C/50 (corresponding to 5 mA g^{-1}). After the rate test, we performed two more stabilization cycles, which yielded 23 cycles in total. After running into the final cut-off condition for charge or discharge, we measured the open circuit voltage (OCV) in each cycle for 10 min before continuing the measurement.

Unless otherwise stated, any specific parameters such as the specific capacity (in mAh g^{-1}) or the specific surface area (in m^2 g^{-1}) are normalized to the CAM mass, and the potential is reported in V vs Li$^+$/Li.

Results and Discussion

Morphology of the as-received CAMs.—As a first step, we will compare qualitatively the morphology of the cathode active

materials on the basis of SEM images. Figure 1 shows the five investigated CAMs from left to right (a−e), whereby the first two rows (1,2) depict top-view images of the pristine CAM powders and the last to rows (3,4) depict cross-sectional images of the pristine, compressed electrodes. At magnifications of 2.500x (1,3) and 10.000x (2,4), the scale bar refers to 5 μm and 1 μm, respectively. The SEM images reveal significant differences between the two porous CAMs (P-wCo-10 (a) and P-woCo-6 (d)) in comparison to the three dense CAMs (D-wCo-10 (b), D-wCo-6 (c) and D-woCo-6 (e)). Here, the top-view images illustrate the size and especially the shape of the secondary agglomerates. While the porous CAMs possess a uniform, almost perfectly spherical shape (see Figs. 1a1 and 1d1), the secondary agglomerates of the dense CAMs are irregularly formed and edged (see Figs. 1b1, 1c1, and 1e1). The higher magnifications reveal some smaller particles on the outer surface of the secondary agglomerates, from which the faceted crystals on the P-wCo-10 CAM can be clearly differentiated from the subjacent material (see Fig. 1a2). These faceted crystals have lateral dimensions of $\approx$0.5 μm and might potentially originate from carbonate impurities, because they were identified as the main impurity on a similar Li- and Mn-rich CAM.[49] Qualitatively, the size of the secondary agglomerates is on the order of $\approx$5–10 μm; a more quantitative assessment was done by dynamic laser scattering, yielding the corresponding D_{50} values that are provided at the top of Fig. 1 and in Table I. These D_{50} values agree within $\approx$1–2 μm with the targeted secondary agglomerate sizes of either 6 μm or 10 μm.

The cross-sectional images were prepared either by mechanical polishing (Figs. 1a3, 1a4, 1b3, 1b4, 1c3, 1c4 for the Co-containing CAMs) or by FIB milling of the cathode electrodes (Figs. 1d3, 1d4,

1e3, 1d4 for the Co-free CAMs). Note that the former approach visualizes only the CAM particles, since the electrodes were embedded into epoxy resin, while in the latter case the C65 conductive carbon also becomes visible between the CAM particles. The cross-sections highlight the interior of the secondary agglomerates. The packing of the primary particles is crucial for the differentiation into porous vs dense CAMs. In case of the porous CAMs (see Figs. 1a3, 1a4, 1d3, and 1d4), the primary crystallites are loosely connected with each other, which gives rise to a fluffy structure with significant void space between the individual crystallites. On the other hand, the dense CAMs are much more closely packed and the crystallites appear to be fused together by solid-solid grain boundaries. While the two Co-containing representatives, D-wCo-10 (see Figs. 1b3, 1b4) and D-wCo-6 (see Figs. 1c3, 1c4), exhibit virtually no void space in their interior, the D-woCo-6 CAM (see Figs. 1e3, 1e4) features some occasional pores, which however might not be connected with each other and/or to the outside.

The qualitative differences observed by SEM imaging find expression in the specific surface areas of the CAMs (A_{BET}). As shown in Fig. 1 and Table I, the A_{BET} values range by a factor of up to $\approx$15, from 5.3–5.4 m^2 g^{-1} for the porous CAMs to 0.37–1.3 m^2 g^{-1} for the dense CAMs. Assuming solid spheres and using the crystallographic density of $\approx$4.35 g cm^{-3}, these A_{BET} values can be translated into an average particle diameter according to $d_{BET} = 6/(\rho_{cryst} \cdot A_{BET})$.[50] In case of the porous CAMs, this diameter amounts to $d_{BET} \approx 0.26$ μm, which is on the order of the primary crystallites (see Figs. 1a4 and 1d4). This estimate seems reasonable. The porous network of the secondary agglomerates enables full access to the inner part of the agglomerates, so that the surface area
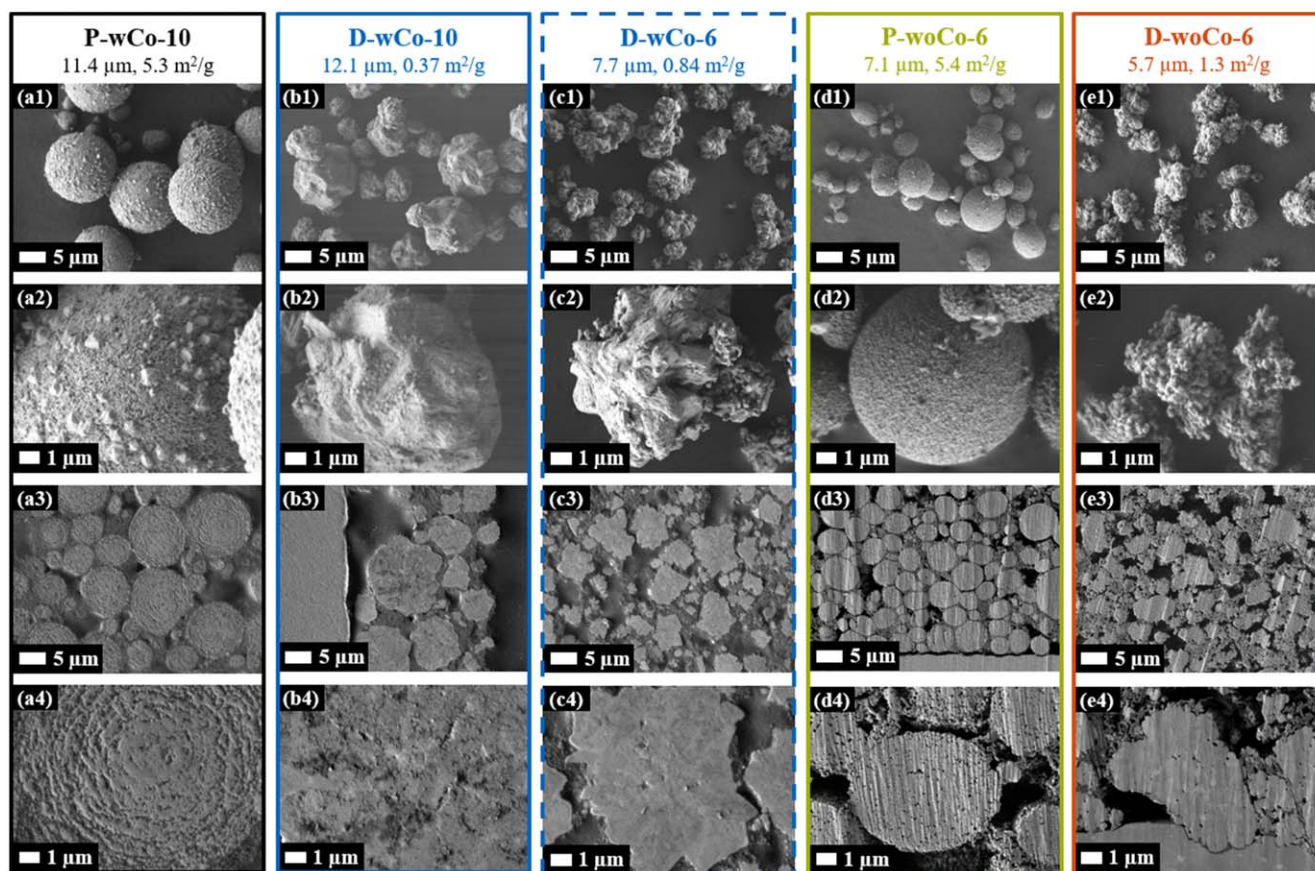

Figure 1. SEM top-view images of the pristine CAM powders (1st and 2nd row) and cross-sectional images of the pristine, compressed electrodes (3rd and 4th row). The cross-sections of the three Co-containing CAMs were prepared by mechanical polishing, while the two Co-free CAMs were treated by FIB milling (see Experimental section). Note that the scratches in the panels (d3, d4, e3, e4) come from the not optimized settings of the FIB milling, and that the internal pore volume of the P-woCo-6 CAM in panel (d4) might be partially smeared and blocked due to abrasion products. The magnifications amount to 2.500x (1st and 3rd row; 5 μm scale bar) and 10.000x (2nd and 4th row; 1 μm scale bar). At the top, the CAM ID is given together with its secondary agglomerate size (given as D_{50} diameter from dynamic laser scattering) and its A_{BET} values (from nitrogen physisorption).

Table 1. Comparison of the five investigated Li- and Mn-rich CAMs with respect to their material properties in the pristine state and their rate test performance. Material properties are the median secondary agglomerate size (D_{50}) from dynamic laser scattering (DLS), the specific surface area (A_{BET}) from N_2 physisorption, the intra-particular pore volume ($v_{pore,intra}$) and porosity (ε_{intra}) from mercury intrusion porosimetry (MIP), as well as the crystallite size (L_{vol}) and microstrain (ε_0) from X-ray powder diffraction (XPD). The discharge capacity of the CAMs is compared at a current density of 1C (corresponding to 250 mA g^{-1}) and at 10 mA m^{-2} (after BET surface area normalization), respectively. The latter was interpolated from the rate test data; except for the D-wCo-10 CAM, which was extrapolated from the lowest current density of ≈14 mA m^{-2}. The reported errors are the standard deviation from at least two measurements (N_2 physisorption and MIP), estimated from a single measurement by the refinement program (XPD), or from two cells averaged over the two cycles at each C-rate (rate test).

| CAM | DLS | N_2 physisorption | MIP | | XPD | | Rate test | |
| | | | | | | | Discharge capacity [mAh g^{-1}] | |
	D_{50} [μm]	A_{BET} [m^2 g^{-1}]	$v_{pore,intra}$ [mm^3 g^{-1}]	ε_{intra} [%]	L_{vol} [nm]	ε_0 [%]	@ 1C	@ 10 mA m^{-2}
P-wCo-10	11.4	5.3 ± 0.2	70 ± 0.3	23.3 ± 0.1	128 ± 7	0.025 ± 0.001	222 ± 1	≈250
D-wCo-10	12.1	0.37	<1	<0.4	too large	0.181 ± 0.003	86 ± 1	(≈180)
D-wCo-6	7.7	0.84	1.8 ± 0.2	0.8 ± 0.1	too large	0.167 ± 0.003	115 ± 1	≈181
P-woCo-6	7.1	5.4 ± 0.3	44 ± 0.5	16.1 ± 0.2	97 ± 6	0.038 ± 0.002	198 ± 1	≈223
D-woCo-6	5.7	1.3 ± 0.04	6.1 ± 0.8	2.6 ± 0.3	too large	0.097 ± 0.001	152 ± 1	≈212

of all of the primary crystallites is exposed to the gas (during the gas physisorption measurement). This, presumably, also allows full access of the primary particle surfaces to the electrolyte (which infiltrates the internal pores when assembled into a battery). In contrast, the average BET-based diameter of the dense CAMs amounts to ≈3.7 μm for D-wCo-10, ≈1.6 μm for D-wCo-6, and ≈1.1 μm for D-woCo-6, which more closely reflects the size of the secondary agglomerates. Consequently, the dense CAMs expose primarily the outer surface area of the secondary agglomerates to the gas (and thus to the electrolyte). Note that the d_{BET} values of the dense CAMs are smaller than the D_{50} values (by a factor of ≈4–6), likely due to their non-spherical shape and the roughness of their outer surface. This is especially pronounced for the D-woCo-6 CAM, where the primary crystallites can actually be identified in top-view mode (see Fig. 1e2), similarly to the two porous CAMs (see Figs. 1a2 and 1d2); however, they are strongly compacted in the bulk of the agglomerates, as seen in the cross-sectional image (see Fig. 1e4).

The SEM images as well as the BET surface areas revealed large morphological differences between the dense vs porous CAMs. Based on this, we also sought to quantify their internal porosity by mercury intrusion porosimetry. Since mercury has a contact angle greater than 90° and thus does not wet most substances, it has to be forced to fill the open pore space by applying an external pressure. According to the Washburn equation (see Eq. 1 in the Experimental section), the pressure correlates inversely with the pore diameter at which the intruded mercury volume is determined by its capacitance change in the penetrometer stem. This approach can be applied to battery material powders[51] and electrodes.[24,52,53]

Figure 2 shows the porosimetry data of the five CAM powders. The pore volume is depicted as accumulative pore volume (v_{pore}) in panel (a) and as its logarithmic derivative (dv_{pore}/dlogd_{pore}) in panel (b), both plotted vs the pore diameter (d_{pore}) on a logarithmic scale, so that the area under the latter curve directly corresponds to the pore volume within the examined pore diameter range. As the large pores get filled first, the measurement can be divided into three sections. In the first section (see ① in Fig. 2a), the loose CAM powders are compacted without filling any of the pore space in between the secondary agglomerates, which gives rise to a linear increase of the intruded volume. Here, the D-wCo-6 (blue dashed line) and D-woCo-6 CAMs (red solid line) seem to be more loosely packed than the other CAMs. When the secondary agglomerates are arranged in a close packing, mercury starts to fill the inter-particular pore volume in between them at Hg pressures that correspond to diameters below ≈4 μm (see section ② in Fig. 2a). The pore diameter at which the peak of the differential volume has its maximum ($d_{pore,inter,max}$) clearly increases with the D_{50} diameter of the secondary agglomerates (listed Table I). The D_{50}/$d_{pore,inter,max}$ ratio amounts to ≈3.5–4.2, which agrees well with the rule of thumb
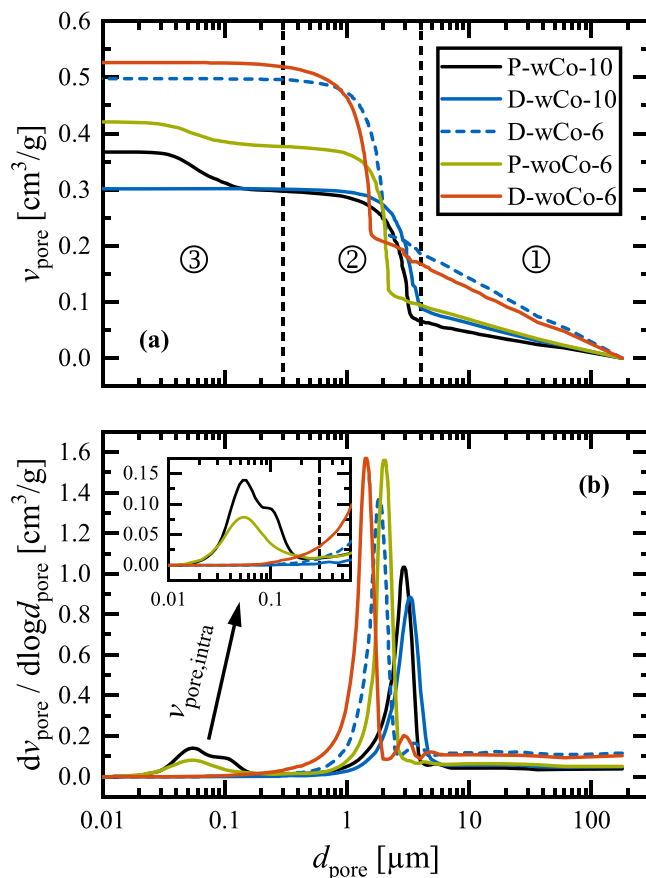

Figure 2. Mercury intrusion porosimetry of the as-received CAM powders. (a) Cumulative pore volume (v_{pore}), and (b) logarithmic differential pore volume (dv_{pore}/dlogd_{pore}) as a function of the pore diameter (d_{pore}) plotted on a logarithmic scale. Starting with large pores, the measurement can be divided into three sections: ① powder compaction, ② filling of inter-particular pores between the secondary agglomerates, and ③ filling of intra-particular pores inside the agglomerates, which is defined as occurring below 300 nm. We show here one measurement for each CAM, while the intra-particular pore volume and porosity reported in Table I are based on two measurements each.

reported by Giesche, namely that the effective pore size between particles is ≈2–4 times smaller than the particle diameter (the exact ratio depends on the particles packing structure).[54]
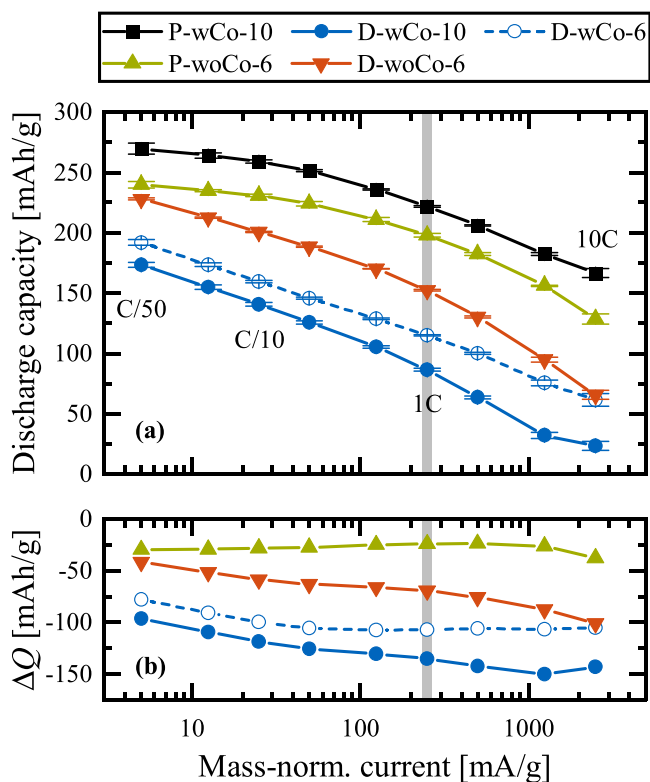
Figure 3. Discharge rate test of the five investigated Li- and Mn-rich layered oxides. After activation and two more stabilization cycles, the CAMs were cycled between cathode potentials of 2.0–4.7 V vs Li$^+$/Li (controlled against a Li-RE), increasing the C-rate in nine steps from 10C to C/50 during discharge, while the charge was limited to ⩽C/2 (with an additional CV hold at 4.7 V to C/50). The two cycles acquired at each C-rate were averaged for this plot from two cells measured for each CAM. The C-rate is referenced to a nominal capacity of 250 mAh g^{-1}, corresponding to a mass-normalized current of 250 mA g^{-1} at 1C. (a) Discharge capacity and (b) capacity difference (ΔQ) relative to the best-performing P-wCo-10 CAM (both in mAh/g). The discharge capacity at 1C (marked by the gray bar) is listed in Table I.

After filling the entire void volume between the agglomerates, further increasing the mercury pressure finally leads to its penetration into the intra-particular pores inside the agglomerates (see section ③ in Fig. 2a). We defined this process as occurring at pore diameters smaller than 300 nm, because the differential pore volume of the porous CAMs (P-wCo-10 (in black) and P-woCo-6 (in green) in Fig. 2b), has a minimum at this diameter between sections ② and ③ (see inset). The pore diameter of the two porous CAMs ranges from ≈200 nm down to ≈20 nm, with a median value of ≈60 nm. Based on the cross-sectional images of the porous CAMs (see Figs. 1a4 and 1d4), the large pores might mainly occur close to the surface of the secondary agglomerates, while the pores become smaller towards their interior. From the intra-particular pore volume ($v_{pore,intra}$) in section ③, we can calculate the internal porosity (ε_{intra}) according to Eq. 2, which amounts to ≈23% and ≈16% for P-wCo-10 and P-woCo-6, respectively (see Table I). The difference of ≈7% is in qualitative agreement to the cross-sectional images, because the P-wCo-10 CAM (Figs. 1a4) appears visually to be more porous than the P-woCo-6 CAM (Fig. 1d4). On the other hand, the three dense CAMs (in blue and red) feature barely any pores below 300 nm, which gives rise to the horizontal plateaus of the mercury intrusion curves in Fig. 2a. The internal porosity of the dense CAMs is less than 3%; the actual value is likely lower due to the artefact arising from an apparent minor filling of inter-particular pores at mercury pressures corresponding to pore sizes below 300 nm (see, e.g., red line of D-woCo-6 in the inset of Fig. 2b). Please note that we defined

the detection limit of $v_{pore,intra}$ to be 1 mm^3 g^{-1}, which is why the upper limit of ε_{intra} is given as 0.4% for D-wCo-10 in Table I.

As discussed in our previous publication,[24] the internal porosity of porous secondary agglomerates leads to a substantially reduced electrode density, which compromises the volumetric energy density of the battery cell. For example, considering that cathode electrodes of densely packed CAMs can typically be calendered to ≈30% porosity,[1,55,56] with the porosity almost entirely due to the pore space between secondary agglomerates (i.e., $\varepsilon^*_{total} \approx \varepsilon^*_{inter} \approx 30\%$), the electrode density of the here examined dense D-woCo-6 CAM at 92.5 wt% CAM in the electrode would be ≈2.69 g$_{electrode}$ cm^{-3}$_{electrode}$ (with $\varepsilon^*_{total} = \varepsilon^*_{inter} + \varepsilon^*_{intra} \approx 32\%$). On the other hand, the electrode density would be only ≈2.22 g$_{electrode}$ cm^{-3}$_{electrode}$ for the porous P-woCo-6 counterpart with an internal porosity of $\varepsilon^*_{intra} \approx 14\%$ ($\varepsilon^*_{total} \approx 44\%$). The asterisk (*) indicates that these porosities are related to the entire electrode and not only to the CAM (see explanation and underlying equations in the Appendix). This comparison illustrates the negative impact of the internal porosity of secondary CAM agglomerates on the achievable electrode density and thus on the potential volumetric energy density of the cell.[51]

Rate test analysis.—Let us now turn towards the electrochemical characterization of the five CAMs. Figure 3 shows the results of a discharge rate test, which was conducted after the first activation cycle (see Fig. A·1 in the Appendix) and two more stabilization cycles (measuring details can be found in the Experimental section). The applied C-rates cover more than two orders of magnitude, from 10C to C/50, whereby 1C corresponds to a mass-normalized current of 250 mA g^{-1}. To avoid any capacity drop due to the kinetic overpotential of the lithium counter-electrode, especially at high C-rates (up to ≈18 mA cm^{-2} at 10C), the cathode potential was controlled vs a lithium reference-electrode between 2.0 and 4.7 V. Furthermore, the use of two glass-fiber separators with a thickness of ≈400 μm prevents an internal short due to lithium dendrites, and the concomitant electrolyte excess (≈13 g$_{electrolyte}$/g$_{CAM}$) avoids the deterioration of the bulk electrolyte due to its continuous reduction on the anode side. Since slow cycles have a higher charge throughput, they are expected to cause more degradation of the CAM, e.g., due to surface reconstruction[20] and impedance build-up.[57] Therefore, the fast rates were performed first, and the decreasing C-rates in the subsequent cycles counteract any potential impedance build-up, so that the entire test procedure represents in good approximation the initial material performance. The charge rate was the same as the discharge rate for ⩽C/2 and was kept at C/2 for higher discharge rates; the charge process was completed by a constant voltage hold at 4.7 V until the current dropped below C/50. This procedure ensures that the upper state of charge (SOC) limit and thus the starting point of each discharge are fairly constant during the rate test. To validate this, we added a 10 min. OCV phase after each charge and discharge step. The last OCV value after running into the upper cathode cut-off potential of 4.7 V was found to only vary within a small voltage window of ≈40 mV for each CAM, i.e., the uppermost SOC is indeed very similar throughout the entire rate test (ΔSOC estimated to be ⩽3 mAh g^{-1}). In contrast, the lower SOC limit after reaching the cathode potential of 2.0 V results in, as expected, lower open circuit voltages when decreasing the C-rate, and the OCV values in the discharged state span over more than 1 V.

As shown in Fig. 3, the porous Co-containing P-wCo-10 CAM (in black) has the best rate capability, reaching capacities from ≈166 mAh g^{-1} at 10C to ≈270 mAh g^{-1} at C/50, which agrees with similar state-of-the-art Li- and Mn-rich layered oxides that have a high BET surface area and contain cobalt.[24,58] On the other hand, the dense Co-containing D-wCo-10 CAM (solid blue line) exhibits the worst performance with only ≈23 mAh g^{-1} at 10C and ≈173 mAh g^{-1} at C/50, whereby the other dense Co-containing D-wCo-6 CAM shows only slightly better performance (dashed blue
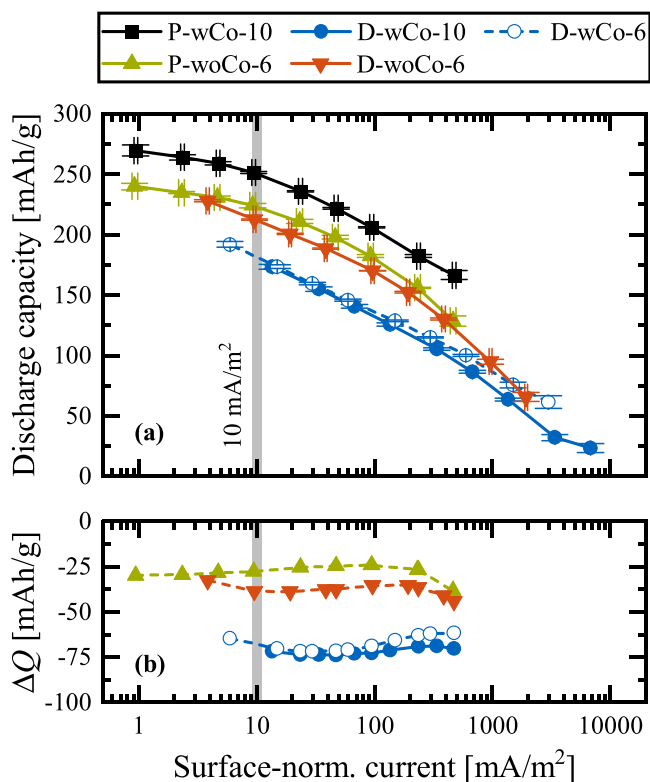
Figure 4. Rate test data of Fig. 3 re-plotted as function of the surface-normalized current, which is calculated by dividing the mass-normalized current by the BET surface of the different CAMs. (a) Discharge capacity and (b) capacity difference (ΔQ) relative to the best-performing P-wCo-10 CAM (both in mAh/g). The discharge capacity at a surface-normalized current of 10 mA m^{-2} (see gray bar) is obtained by interpolation of the available data points and is listed in Table I.

line). Since the performance of the Co-free CAMs (P-woCo-6 (in green) and D-woCo-6 (in red)) falls in between these three Co-containing CAMs, there is no obvious correlation between the accessible capacity and whether the CAMs contain cobalt or not. On the other hand, the performance of the CAMs seems to be sorted according to their BET surface area (see Table I): the porous CAMs with BET surface areas of more than 5 m^2 g^{-1} (P-wCo-10 and P-woCo-6) have the highest capacities, followed by the dense CAMs, whose capacities decrease with decreasing BET surface area, namely from D-woCo-6 with 1.3 m^2 g^{-1} to D-wCo-6 with 0.84 m^2 g^{-1}, all the way to D-wCo-10 with 0.37 m^2 g^{-1}. Furthermore, the capacity difference of the dense CAMs relative to the porous CAMs decreases as the applied C-rate becomes smaller, which is illustrated by the plot of the capacity difference of any given CAM relative to the best-performing P-wCo-10 CAM in Fig. 3b. The observed decrease of performance with decreasing BET surface area is not too surprising, as higher BET values result in more CAM surface area that is available for lithium-ion transfer across the CAM/electrolyte interface, based on the assumption that the CAM surface area measured by N$_2$ physisorption equals the CAM surface area that is exposed to the electrolyte during the rate test (see below discussion). This holds true as long as micropores below ≈1 nm do not contribute significantly to the BET surface area, as those could only be accessed by the nitrogen gas during BET measurements and not by solvated lithium-ions during electrochemical measurements.[59]

The current divided by the CAM surface area exposed to the electrolyte (further on referred to as the surface-normalized current) defines the actual current density that governs the charge-transfer process. Thus, assuming that the intrinsic charge-transfer resistance referenced to the CAM/electrolyte interfacial surface area (in units

of Ω·m^2) is similar for the different CAMs, their effective charge-transfer resistance (in units of Ω·g) should scale linearly with their BET surface area. As the porous CAMs feature the highest BET surface area (i.e., the highest surface-to-bulk ratio), with the majority of the primary crystallites being in direct contact with the electrolyte, their effective charge-transfer resistance (in units of Ω·g) should be the lowest. On the other hand, in case of the dense CAMs, the primary crystallites are fused together through solid-solid grain boundaries, such that only the outer surface of the secondary agglomerates is exposed to the electrolyte. This in turn increases their effective charge-transfer resistance (in Ω·g), which leads to higher overpotentials at a given C-rate. Consequently, the rate test representation in Fig. 3 is not a fair comparison between the investigated CAMs, because the mass-normalized current (in mA/g) at a given C-rate does not account for the largely different CAM/electrolyte interfacial areas. Therefore, under the reasonable assumption that the intrinsic charge-transfer resistance (in units of Ω·m^2) is similar, the rate capability of the CAMs should be compared as a function of the surface-normalized current (in units of mA/m^2), rather than in terms of the mass-normalized current or C-rate (as was done in Fig. 3).

Such a comparison is shown in Fig. 4, where the mass-normalized current (from Fig. 3) is divided by the BET surface area of the CAMs, plotting the discharge capacities against the logarithm of the surface-normalized current. Now, the rate test data of the different CAMs are shifted along the x-axis: the porous CAMs reach lower surface-normalized currents (shifted to the left) than the dense CAMs (shifted to the right). This has some interesting implications. The dense and Co-containing CAMs (in blue), which differ just by agglomerate size (12.1 μm for D-wCo-10 vs 7.7 μm for D-wCo-6, see Table I), now exhibit the same discharge capacity for most of the shared surface-normalized current range in Fig. 4, while they were separated by ≈20–40 mAh g^{-1} at any given C-rate (see Fig. 3b). This means that the BET surface area (different by a factor of ≈2.3) can quantitatively explain their performance variation. In a similar manner, the performance difference between the two Co-free CAMs (P-woCo-6 (in green) and D-woCo-6 (in red)) is almost entirely compensated for by the surface area normalization (different by a factor of ≈4.2).

The porous and Co-containing P-wCo-10 CAM (in black) still outperforms the other CAMs, but the capacity offset is nearly constant within the surface-normalized current range that the materials have in common, as shown by plotting the capacity difference of the various CAMs with respect to the best-performing P-wCo-10 CAM (see Fig. 4b). There are some small deviations at high surface-normalized currents (corresponding to the two highest C-rates of 5C and 10C), where the capacity is not only governed by the CAM itself, but also by electrode properties such as loading and tortuosity. For example, the capacities of the Co-free CAMs (with ≈6.5–7.0 mg$_{CAM}$ cm^{-2} loading) decrease faster with increasing rate compared to the Co-containing CAMs (with ≈5.0–6.0 mg$_{CAM}$ cm^{-2} loading) due to their higher loading. The remaining offset between the CAMs indicates at least a second, yet unknown descriptor of their electrochemical performance, but the surface area obviously plays a big role. Looking at a practically relevant C-rate of 1C (see gray bar in Fig. 3), the best- and the worst-performing CAMs, i.e., P-wCo-10 and D-wCo-10, are separated by ≈136 mAh g^{-1}. After surface area normalization, the capacity offset is almost halved to ≈70 mAh g^{-1} at essentially all surface-normalized currents (see solid blue symbols in Fig. 4b). A similar reduction is achieved for the other dense CAMs, as can be checked in Table I, where the capacity values at 1C (≡ 250 mA g^{-1}) and at 10 mA m^{-2} (see gray bar in Fig. 4a) are summarized for all the here investigated CAMs.

Prior to concluding this discussion, it must be mentioned that the here used surface-normalized currents are based on the BET surface area of the as-received CAM powders, even though the actual CAM/electrolyte interfacial surface area during the rate test might increase to somewhat higher values, as reported by Oswald et al. for stoichiometric NCMs.[59] The extent of surface area increase over
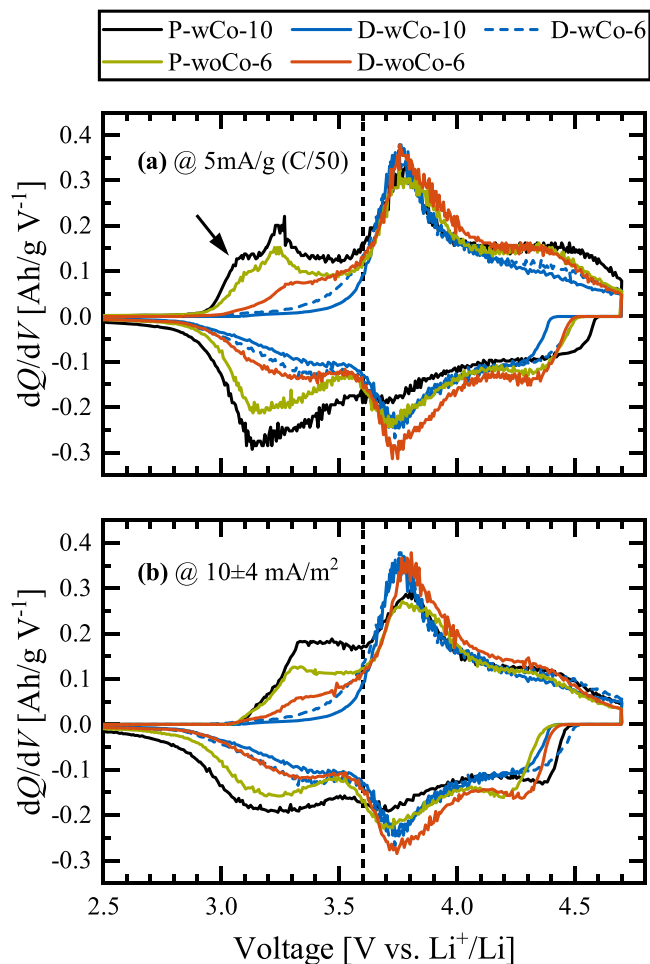
Figure 5. Differential capacity (dQ/dV) of the investigated CAMs, as measured during the rate test in Fig. 3. The CAMs are compared at two different conditions: (a) at the slowest C-rate of C/50, corresponding to a mass-normalized current of 5 mA g^{-1}, or (b) at a fixed surface-normalized current of $\approx$10 mA m^{-2}, which corresponds to different C-rates for each CAM due to their different surface areas (i.e., C/5 for P-wCo-10 and P-woCo-6, C/20 for D-woCo-6, and C/50 for D-wCo-10 and DwCo-6). The dashed vertical line separates the low-voltage redox feature below 3.6 V from the redox features at higher voltages. The arrow in panel (a) highlights the dQ/dV peak of a spinel layer formed around the primary particles of the porous CAMs.

the course of the test procedure (with in total 23 cycles) was examined for a porous (P-woCo-6) and a dense CAM (D-woCo-6), using the capacitance-based method developed by Oswald et al.[59] As this revealed a similar surface area increase of the porous and the dense CAM (by a factor of $\approx$1.4–1.6; see Appendix), the conclusions drawn from Fig. 4 still hold true (only the absolute numbers of the surface-normalized currents would change by this factor).

In order to understand where the remaining capacity offset comes from, Fig. 5 shows dQ/dV data of the CAMs during the rate test shown in Fig. 3. They are compared both at the slowest C-rate of C/50, corresponding to a mass-normalized current of 5 mA g^{-1} (see Fig. 5a), and at a similar surface-normalized current of $\approx$10 mA m^{-2} (see Fig. 5b). Due to the largely different CAM surface areas, the latter comparison translates into different C-rates, ranging from C/5 for the high surface area CAMs to C/50 for the low surface area CAMs. Note that the surface-normalized representation is not freely chosen (due to the pre-defined C-rates in the rate test and the different CAM surface areas), but the variation of the surface-normalized current amounts to less than 10 ± 4 mA m^{-2}. We show both representations of the dQ/dV data, because the yet unknown

descriptor(s) of the accessible capacity do not necessarily have the same dependence on the effective CAM particle diameter that was implied by the above analysis based on surface-normalized currents. There, we had assigned the origin of the different observed capacities to the charge-transfer resistance, which differs at a given C-rate (in units of $\Omega \cdot$g), but which is expected to be identical in its intrinsic unit after surface area normalization (in units of $\Omega \cdot$m^2). Assuming spherical particles (reasonably consistent with the SEM images in Fig. 1), the surface area scales inversely with the effective particle diameter (i.e., $d_{particle}$ based on the actual CAM/electrolyte interfacial area), which suggests the following proportionality between the accessible capacity (Q) and $d_{particle}$: $Q \propto 1/R_{CT} \propto A_{BET} \propto 1/d_{particle}$. In case of the porous CAMs, the effective particle diameter corresponds to the primary crystallite size (on the order of $\approx$230–240 nm, as deduced from the A_{BET} values), whereas the dense CAMs only expose the outer surface of the secondary agglomerates to the electrolyte, so that the effective particle diameter is similar to their D_{50} values of $\approx$6–12 μm. Since the relevant particle diameters differ by more than one order of magnitude, it is not unreasonable to assume that the remaining capacity offset between the different CAMs at a given surface-normalized current (see Fig. 4b) might be explained by their solid-state lithium diffusion kinetics. Here, the effective diffusion time ($\tau_{diffusion}$) would scale with the solid-state lithium diffusion coefficient ($\tilde{D}_{Li}$) according to $\tau_{diffusion} = d_{particle}^2/(4\tilde{D}_{Li})$.[60,61] For the same lithium diffusion coefficient ($\tilde{D}_{Li}$), the different diffusion lengths from the surface into the core of the CAM particles (i.e., $d_{particle}/2$) result in different diffusion times, so that the accessible capacity might also have an additional dependence on the particle diameter according to $Q \propto 1/\tau_{diffusion} \propto 1/d_{particle}^2$.

We will revisit this topic; however, let us start by analyzing the dQ/dV data in Fig. 5. They can be divided into three regions: a broad low-voltage feature up to $\approx$3.6 V, followed by a sharp, well-defined and large peak at $\approx$3.8 V, which is completed by another broad high-voltage feature positive of $\approx$4.1 V. Independent of the two different dQ/dV comparisons (i.e., either at equal C-rate (Fig. 5a) or at equal surface-normalized current (Fig. 5b)), the investigated CAMs differ predominantly with respect to their low-voltage feature (on the left-hand side of the dashed vertical line), which is virtually absent for the D-wCo-10 CAM (solid blue line), but strongly pronounced for the P-wCo-10 CAM (solid black line). The low-voltage features of the other CAMs fall in between these two extreme cases.

Assat at al. used a series of spectroscopic techniques to investigate Li[Li$_{0.20}$Ni$_{0.13}$Co$_{0.13}$Mn$_{0.54}$]O$_2$, which features the same morphology and dQ/dV characteristics as our porous CAMs.[62] By doing so, they managed to assign the different voltage regions to specific redox activities and thus to clarify the charge compensation mechanism of post-activated Li- and Mn-rich CAMs (i.e., after their first activation cycle). The oxygen redox (O^{2-}/O^{n-} with n < 2) is spread over the entire voltage regime, accounting exclusively for the high-voltage feature, but being mixed in different ratios with the cationic redox for the other dQ/dV peaks. The sharp and large peak at $\approx$3.8 V can mainly be ascribed to the redox activity of Ni (Ni^{2+}/Ni^{3+}/Ni^{4+}) and, if present, of Co (Co^{3+}/Co^{4+}). Mn is originally in its inactive 4 + state in the pristine Li- and Mn-rich layered oxide, but the oxygen redox initiates some Mn redox activity (Mn^{3+}/Mn^{4+}) after activation ($\approx$10% Mn^{3+} in the discharged state according to Assat et al.[62]), which further grows during long-term cycling.[63] This Mn redox and the accompanied anionic redox of oxygen take place in the low-voltage feature negative of $\approx$3.6 V.

Please note that the porous CAMs (P-wCo-10 (in black) and P-woCo-6 (in green)) show an additional shoulder at $\approx$3.0–3.15 V during charge at the lowest C-rate of C/50 (highlighted by the arrow in Fig. 5a). As reported by Teufl et al.,[20] this shoulder is distinctive of a spinel-like layer which is formed at the surface of the particles. Initiated by oxygen release at the end of the activation charge (see also discussion of Fig. A·1), the oxygen-depleted layered surface

Table II. Estimation of the characteristic diffusion time for the five as-received CAMs and the post-calcined D-woCo-6-1000C CAM according to $\tau_{\mathrm{diffusion}} = d_{\mathrm{particle}}^2/(4\tilde{D}_{\mathrm{Li}})$. Here, the particle diameter is derived from their BET surface area according to $d_{\mathrm{particle}} \approx d_{\mathrm{BET}} = 6/(\rho_{\mathrm{cryst}} \cdot A_{\mathrm{BET}})$ with $\rho_{\mathrm{cryst}} \approx 4.35$ g cm^{-3}, and the solid-state lithium diffusion coefficient is assumed to be $5 \cdot 10^{-14}$ cm^2 s^{-1} for all CAMs. The materials are ordered by their BET surface area from low to high A_{BET} values, and the comparison also includes their microstrain ε_0.

CAM	A_{BET} [m^2/g]	d_{BET} [μm]	$\tau_{\mathrm{diffusion}}$ [h]	ε_0 [%]
D-wCo-10	0.37	$\approx$3.7	$\approx$190	0.181
D-woCo-6-1000C	0.68	$\approx$2.0	$\approx$57	0.038
D-wCo-6	0.84	$\approx$1.6	$\approx$37	0.167
D-woCo-6	1.3	$\approx$1.1	$\approx$16	0.097
P-wCo-10	5.3	$\approx$0.26	$\approx$0.94	0.025
P-woCo-6	5.4	$\approx$0.26	$\approx$0.91	0.038

gradually transforms into a resistive, spinel-like layer within the first $\approx$20 cycles (the C/50 data shown in Fig. 5a corresponds to cycle 21 of the test procedure). The spinel feature is visible for the porous CAMs, since all primary particles are exposed to the electrolyte, yielding a relatively high surface spinel fraction (maximum of $\approx$5 mol% and layer thickness of $\approx$2 nm for the here investigated CAMs with $\delta = 0.14$).[20] For the dense CAMs, the spinel phase can be formed only at the outer surface of the secondary agglomerates, which results in a negligibly small spinel fraction. However, the spinel surface feature is small compared to the following bulk feature from Mn and O redox and is therefore not taken into consideration for the further analysis.

The presence (or absence) of specific redox activities points towards a bulk property of the CAMs as being the second descriptor of their electrochemical performance. This brings us back to the above discussion about the solid-state lithium diffusion. Croy and co-workers came to a similar conclusion, when they were investigating in detail the impedance characteristics of Li- and Mn-rich layered oxides,[64] e.g., by changing the particle morphology through the calcination conditions.[65] While the impedance at voltages greater than $\approx$3.6 V ($\approx$3.5 V in their studied full-cells) is dominated by the CAM/electrolyte interface,[65] the distinct impedance rise at voltages smaller than $\approx$3.6 V is ascribed to local structural changes in the bulk of the CAM particles. These changes are associated with low-voltage, disordered lithium sites with slow lithium diffusion.[64] Here, the authors were also emphasizing the influence of the particle size, which affects the effective diffusion time to the second power ($\tau_{\mathrm{diffusion}} = d_{\mathrm{particle}}^2/(4\tilde{D}_{\mathrm{Li}})$).

In order to roughly estimate the diffusion time of the five cathode active materials, we use the average BET-based particle diameter that differs by a factor of $5.4/0.37 \approx 15$ for the end members P-woCo-6 and D-wCo-10, or squared by a factor of $(5.4/0.37)^2 \approx 210$ (see A_{BET} and the thereof derived d_{BET} in Table II). The SOC-dependent lithium diffusion coefficient can be determined from various techniques, including the galvanostatic intermittent titration technique (GITT),[60,66] electrochemical impedance spectroscopy (EIS),[50,62] and cyclic voltammetry[67,68]; however, the reported values of $\tilde{D}_{\mathrm{Li}}$ span over several orders of magnitude from $\approx$10^{-11} to $\approx$10^{-18} cm^2 s^{-1} for Li− and Mn-rich layered oxides. This huge scatter is a well-known problem in the literature,[61,69] and we select a median value of $\tilde{D}_{\mathrm{Li}} \approx 5 \cdot 10^{-14}$ cm^2 s^{-1} for our calculation, which results in reasonable diffusion times as shown in Table II.

The characteristic diffusion time of the lithium-ions from the surface into the core of the particles (or in the reverse direction) ranges from $\approx$190 h for the D-wCo-10 CAM to only $\approx$1 h for the two porous CAMs. Consequently, the extent of the low-voltage redox feature below 3.6 V might be solely explained by the effective particle size, because the diffusion time of the D-wCo-10 CAM exceeds the available charge/discharge time at the lowest C-rate of

C/50 during the rate test, which is why the low-voltage peak is virtually absent in the dQ/dV plots (see solid blue line in Fig. 5). On the other hand, the two porous CAMs could be operated until 1C without any diffusion limitation, resulting in a pronounced low-voltage peak at lower C-rates (see black and green lines in Fig. 5). Since the other CAMs line up in between, we assume a correlation between the increasing low-voltage redox peak and the decreasing diffusion time. The latter seems in turn to scale with the effective particle diameter. Note that the diffusion coefficient increases at higher SOCs (i.e., in the delithiated state) by a factor of $\approx$10–100,[50,62,66] so that the redox features at higher voltages are considerably less affected by the solid-state lithium diffusion kinetics.

In order to prove the particle size effect for the same base material, we performed a post-calcination of the D-woCo-6 CAM at 1000 °C for 5 h in argon atmosphere (see Experimental section for further details). As expected, the BET surface area of the D-woCo-6-1000C CAM is roughly 2-fold lower than that of the as-received parent due to particle growth, and the diffusion time would thus increase by a factor of $\approx$4 (see Table II). The rate test performance of both CAMs is compared in Fig. 6.

Surprisingly, the post-calcined CAM (dashed blue line in Fig. 6b) outperforms the as-received CAM (solid blue line in Fig. 6b) during the entire rate test. The improvement of the discharge capacity amounts to $\approx$66 mAh g^{-1} at the highest C-rate of 10C and still to $\approx$13 mAh g^{-1} at the lowest C-rate of C/50, respectively. Please note that the capacity increase would be even higher in the representation vs the surface-normalized current, as the curves are shifted along the x-axis. This unexpected trend is, at first glance, contradicting the results of Liu et al.[60] and Gutierrez et al.,[65] who observed lower capacities for CAMs calcined at higher temperatures compared to those calcined at lower temperatures.

To gain a detailed insight, Fig. 6a compares the discharge dQ/dV data of both CAMs. Focusing on the low-voltage redox peak below 3.6 V (on the left-hand side of the dashed vertical line), there are rate-dependent differences between the as-received CAM (solid lines) and the post-calcined CAM (dashed lines): (i) at C/50 (in red), the capacity share of D-woCo-6-1000C is higher than that of D-woCo-6 (see the plain area with the "+" sign); (ii) at C/2 (in green), both curves lie on top of each other; and (iii) at 2C (in blue), D-woCo-6-1000C contributes less capacity than D-woCo-6 (see the hatched area with the "–" sign). Due to the simultaneous changes at higher voltages, we can probably obtain more authoritative information by comparing the capacity contributions above ($Q_{>3.6V}$, green lines) and below 3.6 V ($Q_{<3.6V}$, red lines) for all C-rates in Fig. 6b. At the lowest C-rate of C/50, the $\approx$13 mAh/g higher capacity of the D-woCo-6-1000C CAM originates indeed mainly from the low-voltage peak ($\Delta Q_{<3.6V} \approx 9$ mAh g^{-1} vs $\Delta Q_{>3.6V} \approx 4$ mAh g^{-1}). Both capacity shares decrease moderately with increasing C-rate; however, starting at $\approx$C/2 for the as-received CAM or at $\approx$2C for the post-calcined CAM, $Q_{>3.6V}$ collapses, while $Q_{<3.6V}$ rises again. This is most likely a resistance effect that shifts dQ/dV features at higher voltages gradually to lower voltages during discharge. As a consequence, the clear distinction between the redox features associated with $Q_{>3.6V}$ and $Q_{<3.6V}$ becomes blurred at high C-rates.

All in all, the results from Fig. 6 question the above-assumed particle size effect on the diffusion kinetics, because the as-received D-woCo-6 CAM and the post-calcined D-woCo-6-1000C CAM ought to be interchanged during the rate test. Alternatively, there might be an additional variation of the lithium diffusion coefficient that was yet assumed to be constant among the tested CAMs. This is exactly what was reported by Liu et al. for their Li[Li$_{0.13}$Ni$_{0.30}$Mn$_{0.57}$]O$_2$ CAMs, which were calcined at sintering temperatures of either at 800, 900, or 1000 °C.[60] Increasing the sintering temperature reduced the BET surface area (from $\approx$5.0 to $\approx$0.68 m^2 g^{-1}) and increased the primary particle size (from diameters of $\approx$80 to $\approx$500 nm); however, at the same, they observed an increase of the lithium diffusion coefficient by GITT (e.g., from $\approx$1.3$\cdot$10^{-15} to $\approx$1.8$\cdot$10^{-14} cm^2 s^{-1} at 4.0 V during charge). The
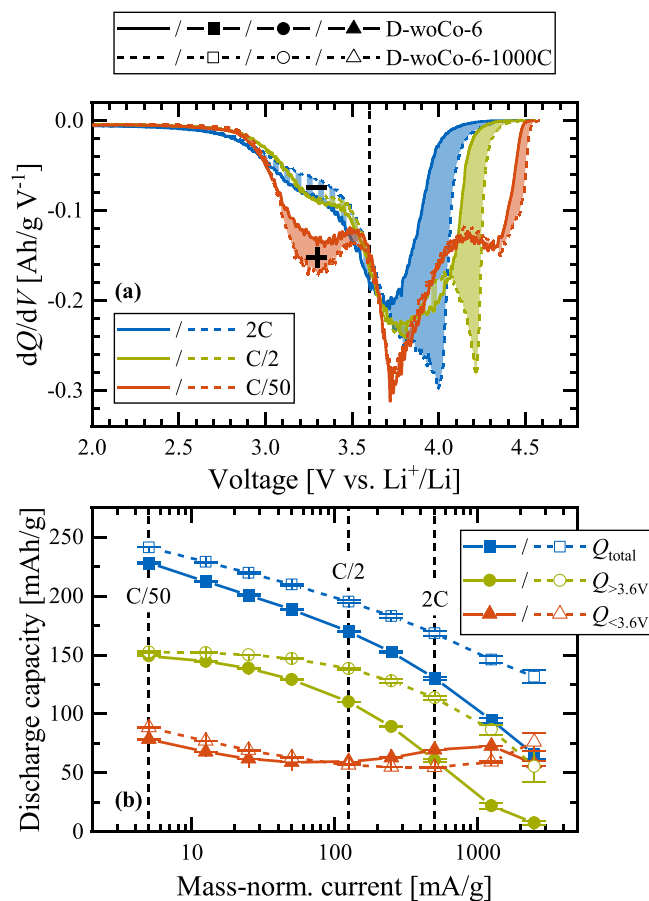
Figure 6. Rate test comparison of the as-received D-woCo-6 CAM and the post-calcined D-woCo-6-1000C CAM, which was heat-treated at 1000 °C for 5 h in argon atmosphere (see Experimental section). (a) Differential capacity (dQ/dV) of the discharge reaction at three different C-rates (viz, at 2C, C/2, and C/50). The capacity difference between both CAMs at a given C-rate is highlighted by the filled area of the same color. The plain area (see also the "+" sign) indicates a higher capacity share of the post-calcined compared to the as-received CAM, while the hatched area (see also the "–" sign) denotes a lower capacity share in the respective voltage range. (b) Discharge capacity vs the mass-normalized current for all tested C-rates. The C-rates that were analyzed in panel (a) are highlighted by dashed vertical lines. Furthermore, the discharge capacity (Q_{total}) is divided into its contributions above 3.6 V ($Q_{>3.6V}$; right-hand side of the dashed vertical line in panel (a)) and below 3.6 V ($Q_{<3.6V}$; left-hand side of the dashed vertical line in panel (a)).
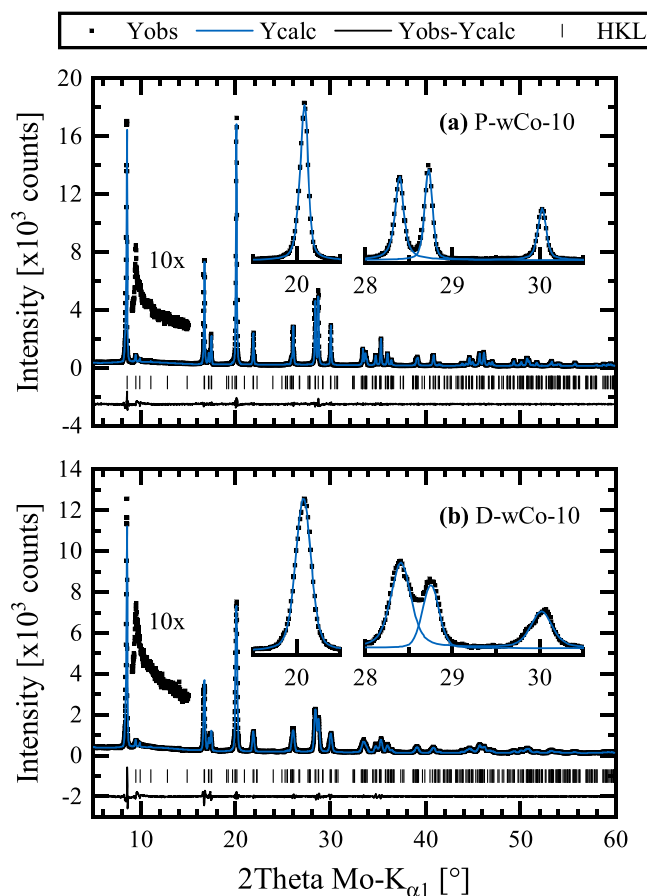

Figure 7. X-ray powder diffractograms of two exemplarily chosen as-received CAM powders acquired on our in-house Mo-diffractometer ($\lambda = 0.7093$ Å), and then refined with a structure-independent fit in the C2/m space group according to the Le Bail method, putting special emphasis on a size/strain analysis of the line broadening (see Experimental section): (a) P-wCo-10, with $R_{wp} = 6.10\%$ and $\chi^2 = 1.70$; (b) D-wCo-10, with $R_{wp} = 6.96\%$ and $\chi^2 = 1.93$. The observed (black points), calculated (blue lines), and difference diffraction profiles (black lines) are shown together with the position of the Bragg reflections (black ticks). The 10x magnifications of the Yobs data points between 9.1–15.0° 2θ highlight the superstructure reflections due to in-plane Li/TM ordering in the TM layer. The insets show a subset of peak which were fitted individually with a pseudo-Voigt peak function (Topas command PV_Peak_Type, using a θ-independent FWHM and Lorentzian-Gaussian mixing parameter for each peak).

authors conclude that the calcination temperature needs to be delicately balanced to obtain the optimum electrochemical performance with respect to these parameters. In their case, the solid-state lithium diffusion kinetics are more slowed down by the increasing particle size at higher temperatures than being accelerated by the increasing lithium diffusion coefficient. Regarding the dense and Co-free CAMs in Fig. 6, $\tilde{D}_{Li}$ has to rise by a factor of greater than 4 to overcompensate the particle growth of the post-calcined compared to the as-received CAM (see Table II). This sounds reasonable considering the ≈16-fold difference of $\tilde{D}_{Li}$ reported by Liu et al.

We want to point out that all these calculations have to be taken with a grain of salt, e.g., due to the approximation of spherical particles and due to the uncertainty of reported $\tilde{D}_{Li}$ values, so that it is impossible to perfectly disentangle the influence of the particle size and the lithium diffusion coefficient. This being said, we assume that the latter is the dominating parameter to explain the remaining capacity differences after surface area normalization in Fig. 4. Since Liu et al. established a connection between $\tilde{D}_{Li}$ and the microstrain

of their investigated CAMs,[60] the following size/strain analysis will provide further evidence for this hypothesis.

Size/strain analysis.—We collected X-ray powder diffraction (XPD) data for every CAM in its pristine state. As an example, Fig. 7 shows the diffractograms of P-wCo-10 and D-wCo-10, which represent the best- and worst-performing of the five as-received CAMs, respectively. All of the CAM powders exhibit a well-defined layered structure, which can be indexed according to the hexagonal α-NaFeO$_2$ structure with $R\bar{3}m$ symmetry.[42,70] The over-lithiation in the TM layer (Li[Li$_\delta$TM$_{1-\delta}$]O$_2$ with $\delta = 0.14 \pm 0.01$) adds an additional honeycomb-like Li/TM ordering, which leads to superstructure reflections (see 10× magnifications between 9.1°–15.0° 2θ in Fig. 7) and allows an alternative indexing in the monoclinic C2/m space group.[48,71] However, the superstructure reflections are quite broad and have a low intensity due to the presence of stacking faults and due to the off-stoichiometric Li/TM ratio.[72,73] The top-view SEM images suggested the presence of surface impurities, especially for the P-wCo-10 CAM (see the faceted crystals on top of the secondary agglomerates in Fig. 1a2). Here, Li$_2$CO$_3$ is a common

Table III. Individual fitting of a selection of peaks from the X-ray powder diffractograms of the P-wCo-10 and the D-wCo-10 CAM shown in Fig. 7 (see insets). The peaks cover one hkl reflection in the R−3m space group, but several in the C2/m space group. The full width at half maximum (FWHM) was determined with a pseudo-Voigt peak function (using the PV_Peak_Type command in Topas).

hbb	*hkl* reflections		FWHM [°]	
	R−3*m*	*C2/m*	P-wCo-10	D-wCo-10
≈20.1	104	20−2, 131	0.0886 ± 0.0006	0.200 ± 0.008
≈28.4	108	13−3, 202	0.106 ± 0.017	0.27 ± 0.03
≈28.7	110	33−1, 060	0.094 ± 0.010	0.22 ± 0.03
≈30.0	113	33−2, 222, 061, 330	0.102 ± 0.016	0.29 ± 0.04

impurity on the CAM surface, as it readily forms under ambient conditions,[49] either from the unreacted lithium source or from leaching lithium out of the layered oxide. Robert et al.[74] and Grenier et al.[75] were able to observe Li_2CO_3 on NCA samples by high-resolution synchrotron XPD, but the most intense (110) reflection at ≈9.8° 2θ (for Mo-$K_{\alpha 1}$ radiation) would be superimposed by the superstructure reflections of over-lithiated samples. Furthermore, we do not observe the (−202) and (002) reflections of Li_2CO_3 at ≈14.0° and ≈14.5°; however, the signal-to-noise ratio and intensity of the laboratory diffractometer is probably too low to resolve impurity phases on the level of less than ≈1 wt%. Therefore, we still assume that carbonate impurities are the most likely source for the faceted crystals observed in the SEM images.

The most interesting observation concerns the line broadening of the reflections. The insets of Fig. 7 show a subset of peaks, which can either be described by one *hkl* reflection in the *R*−3*m* symmetry or by several reflections in the *C2/m* symmetry (see *hkl* assignments in Table III). Already by naked eye, it is obvious that the P-wCo-10 CAM (see Fig. 7a) has much narrower reflections than the D-wCo-10 CAM (see Fig. 7b). This finding is confirmed by an individual fitting of the peaks with a pseudo-Voigt peak function (containing Lorentzian and Gaussian contributions). The full width at half maximum (FWHM) of the peaks (corresponding to either one or two/four reflections) is listed in Table III. The selected peaks of the P-wCo-10 CAM are narrower by a factor of ≈2.3−2.8 than the peaks of the D-wCo-10 CAM, and the FWHM difference becomes larger with increasing 2θ. At a first glance, this result is in contradiction to the SEM images in Fig. 1, because the primary crystallites of the P-wCo-10 CAM are expected to be significantly smaller than that of the D-wCo-10 CAM. According to the well-known Scherrer equation (see Eq. 4), the crystallite size is inversely proportional to the line broadening, i.e., the P-wCo-10 CAM should exhibit broader reflections than the D-wCo-10 CAM. However, the microstrain (ε_0 in Eq. 5) provides a second contribution to the sample broadening, and it is a measure of the lattice imperfection in the bulk of the sample. Both contributions can be separated and quantified by their different θ-dependence. This is typically done by the so-called Williamson-Hall method, where the line broadening is individually analyzed for each reflection (in a similar manner than for the selected peaks in Fig. 7 and Table III).[34,42] Manual analysis is possible only in the *R*-3*m* space group, where each apparent peak belongs to one *hkl* reflection (strictly speaking, this was done above). Therefore, we decided to rely on the whole powder pattern fitting (WPPF) approach,[76] where all reflections can be treated together in a structure-independent fit according to the Le Bail method and which enables the use of the *C2/m* symmetry. Since the *C2/m* space group has more than double the amount of *hkl* reflections than *R*-3*m* for the same set of peaks, it can model their line broadening more accurately. The size/strain analysis, as implemented in the Topas software package,[47] uses the same base equations as the Williamson-Hall analysis (detailed information are provided in the Experimental section).

The applied model describes the observed diffraction patterns very well, as can be seen visually in Fig. 7, and also the error indices R_{wp} and χ^2 (listed in the figure caption) are reasonably low. The size/strain

values of all five as-received CAMs are listed in Table I. We will first focus on the crystallite size parameter L_{vol}, which is defined as the volume-weighted mean column length of the crystallites and which can be converted into an average diameter of $d_{sphere} = 4/3 \cdot L_{vol}$ using a spherical approximation.[37] For all three dense CAMs, the L_{vol} values were too large (i.e., >200 nm) to contribute significantly to the line broadening, and they were therefore excluded from the refinement. On the other hand, the porous CAMs have L_{vol} values of ≈128 nm for P-wCo-10 and ≈97 nm for P-woCo-6, which yield spherical diameters of ≈171 nm and ≈129 nm, respectively. These results are in good qualitative agreement with the SEM images in Fig. 1, and for the porous CAMs, the XPD-based d_{sphere} values agree within a factor of ≈2 with the d_{BET} values of 260 nm approximated from their specific surface areas.

Focusing next on the microstrain parameter, one can observe that the ε_0 values vary by a factor of ≈7 for the different CAMs, viz., from ≈0.025% for the P-wCo-10 CAM to ≈0.181% for the D-wCo-10 CAM (see Table I). This range is consistent with the ε_0 values of layered oxides reported in the literature.[36,60,77] For example, Liu et al. reported ε_0 values ranging from ≈0.13% (at 800 °C) to ≈0.08% (at 1000 °C) for the $Li[Li_{0.13}Ni_{0.30}Mn_{0.57}]O_2$ CAM that was calcined at different sintering temperatures.[60] Using the classical Williamson-Hall approach, Gent et al. measured ε_0 values of ≈0.10% and ≈0.19% for pristine and partially delithiated NCM-111, respectively (the particle size of the poly-crystalline CAM remained fairly constant at ≈200 nm).[77] Fell et al. monitored the microstrain in a similar fashion for the Li- and Mn-rich $Li[Li_{0.2}Ni_{0.2}Mn_{0.6}]O_2$ during the activation cycle (excluding size-induced broadening).[36] Here, the microstrain increased from ≈0.15% in the pristine state to ≈0.32% in the middle of the first discharge. The increase of microstrain during cycling is explained by the growth of crystallographic defects such as vacancies, antisite disorder, dislocations, and stacking faults as well as large scale SOC heterogeneities. Such an increase during cycling is also expected for the here examined CAMs, but assuming that the increase scales with the ε_0 values of the pristine samples, we can try to correlate these initial values with the electrochemical performance of the CAMs. This attempt is motivated by the fact that the best- and worst-performing CAMs during the rate test (i.e., P-wCo-10 and D-wCo-10, see Figs. 3 and 4) also exhibit the lowest and highest microstrain values, respectively. To compensate for the surface area effect on the accessible capacities, Fig. 8 compares the discharge capacities at a given surface-normalized current of either 10 or 100 mA m^{-2} (both datasets were extracted after surface area normalization from Fig. 4) with the microstrain values of the CAMs.

Surprisingly, there is an almost linear relationship between the discharge capacity at a given surface-normalized current and the microstrain, with the discharge capacity decreasing by ≈40 ± 5 mAh g^{-1} per 0.1% increase in microstrain. Since the microstrain goes hand in hand with the effective particle diameter for the as-received CAMs (see Table II), this correlation does not automatically imply causation. Fortunately, the post-calcined D-woCo-6-1000C CAM forms an exception, with d_{BET} increasing from ≈1.1 to ≈2.0 μm, while ε_0 diminishes from ≈0.097% to ≈0.038% as compared to the as-received parent. The post-calcination was
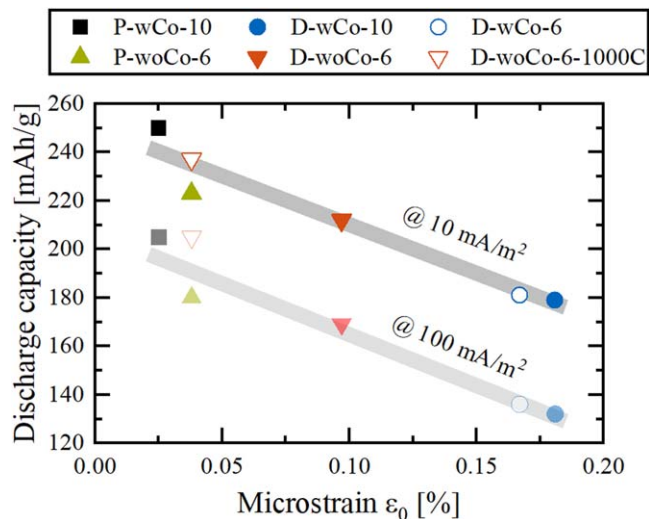
Figure 8. Correlation of the discharge capacity at two different surface-normalized currents with the microstrain of the as-received CAMs and the post-calcined D-woCo-6-1000C CAM. The discharge capacities were extracted at 10 mA m^{-2} (intensively colored data points) and 100 mA m^{-2} (transparent data points) by interpolation of the rate test data in Fig. 4 (please note that the discharge capacity of the D-wCo-10 CAM at 10 mA m^{-2} was extrapolated from the lowest current density of $\approx$14 mA m^{-2}). To illustrate the fairly linear relationship, the gray bars serve as a guide to the eye.

intentionally done at 1000 °C and thus beyond the original sintering temperature of $\approx$930 °C, so that the crystallinity is improved by healing up lattice defects. The post-calcined CAM fits perfectly into the trend lines of the as-received CAMs in Fig. 8 (see red open triangles). Therefore, we are confident that the solid-state lithium diffusion kinetics determine the accessible capacity predominantly according to the following proportionality: $Q \propto 1/\tau_{\text{diffusion}} \propto \tilde{D}_{\text{Li}} \propto 1/\varepsilon_0$. On the other hand, the initially suggested particle size effect is regarded to be of minor importance for the lithium diffusion in the solid phase.

Since the microstrain is a rather generic parameter, we would finally like to address the question which kind of lattice imperfection might be responsible for the observed differences among the here examined CAMs. In case of Li- and Mn-rich layered oxides, the degree of Li/TM ordering in the TM layer (within the *ab*-plane) and their stacking (along the *c*-direction) is an often discussed phenomenon.[72,78,79] However, the comparison of the superstructure region (see 10x magnifications in Fig. 7) reveals no significant differences between the tested CAMs. This leads us to the conclusion that the in-plane Li/TM ordering and the extent of stacking faults is comparable and thus not the main contribution to microstrain. Furthermore, we also performed some Rietveld refinements to evaluate the impact of the Li-Ni mixing (not shown here). Briefly summarized, the Ni amount on the Li layer might differ by up to $\approx$3% among the investigated CAMs; however, we do not observe a causal relationship to the microstrain.

Alternatively, there is increasing attention in the literature to the impact of oxygen vacancies.[27,80–83] Regarding the synthesis of the CAMs, they might play an important role in this work, because the calcination requires the infiltration of lithium and also oxygen into the TM precursors.[9,84] For the dense CAMs, the oxygen atoms thus might have much longer solid-state diffusion pathways than for the porous CAMs to reach the core of the secondary agglomerates, leading potentially to more oxygen vacancies (and consequently to more microstrain). Oxygen vacancies can be also created on purpose after calcination, e.g., chemically by a gas-solid interface reaction with CO_2 (using NH_4HCO_3 as precursor)[80,81] or electrochemically in an electrochemical reactor with a solid electrolyte separator (i.e., cathodically charging a CAM powder bed).[83] Both methods are carried out at temperatures of up to 600 °C and could hence reduce

the available surface area due to agglomeration and grain growth.[83] This makes it difficult to discern the influence of oxygen vacancies from the surface area effect. Apart from that, the results in the literature are ambiguous. After introducing oxygen vacancies in the Co-free CAM Li[Li$_{0.2}$Ni$_{0.2}$Mn$_{0.6}$]O$_{2-z}$, Nakamura et al.[83] measured a slightly lower capacity and rate capability (for $z = 0.03$ vs $z = 0$), while Li et al.[81] observed the opposite trend (for $z = 0.07$ vs $z = 0$). Both studies have in common that the oxygen vacancies enhance the Mn redox feature at low voltages (at the expense of the Ni redox feature at higher voltages). Recently, Csernica et al.[27] quantified the oxygen loss, including bulk oxygen vacancies, from a Li- and Mn-rich layered oxide (with $\delta = 0.18$) upon cycling. After 500 charge/discharge cycles, the authors found $\approx$6.5 at% oxygen vacancies ($\Delta z \approx 0.13$) and they further linked the progressive oxygen release to the voltage fade of the CAM.[27] The so-called voltage fade describes the reduction of the average operating voltage of Li- and Mn-rich layered oxides during electrochemical cycling.[5] In dQ/dV plots, the voltage fade manifests in (i) the redox peak at $\approx$3.8 V gradually shifting to lower voltages and in (ii) the low-voltage feature also moving from $\approx$3.4 to $\approx$3.0 V.[17,27] All these results are in contradiction to our findings, where higher ε_0 values (due to more defects) strongly diminish the low-voltage feature, being virtually absent for the D-wCo-10 CAM with the highest microstrain (see Fig. 5). Thus, oxygen vacancies also seem to be an unlikely origin of microstrain in our present work.

Lastly, we want to discuss the possibility of dislocations that represent line defects by introducing extra half-planes into the lattice.[29] In contrast, the above-discussed stacking faults are classified as planar defects, which perturbs the stacking sequence of the honeycomb-like ordered TM layers along the *c*-axis, while preserving their cubic close-packed arrangement (i.e., O3 packing).[78] Singer et al. could monitor the dislocation density in single particles during cycling by operando 3D Bragg coherent diffractive imaging.[29] They found much more dislocations in the investigated Li- and Mn-rich CAM than in stoichiometric NCA (which was further in accordance with the microstrain values from bulk powder diffraction). Furthermore, the dislocations modify the local lithium environment by perturbing the O3 packing (containing only edge-sharing octahedral sites between the Li and TM layer) and by also introducing O1-like parts (with face-sharing octahedral sites).[29] This defect is another kind of stacking fault, whose energetic penalty slows down the lithium-ion diffusion, particularly at high lithium concentrations (i.e., in the discharged state). However, the authors correlated the dislocations again to the voltage fade in over-lithiated CAMs and thus to the gradual emergence of low-voltage characteristics upon cycling.

Since most of the known lattice defects (including the in-plane Li/TM ordering, stacking faults, oxygen vacancies, and dislocations) seem to contradict our observation that increasing microstrain reduces the capacity contribution at low voltages, we cannot present a conclusive theory about the origin of the microstrain, but we assume it to influence the solid-state lithium diffusion coefficient (governing especially the low-voltage redox feature, as shown in Figs. 5 and 6). Future studies on this topic should include high-resolution (scanning) transmission electron microscopy ((S)TEM) experiments, which are now capable of visualizing even light elements such as lithium and oxygen in layered transition-metal oxides,[85] and which could thus detect all different kinds of lattice imperfections on an atomic level.[31]

In summary, we could show that the BET surface area and the bulk microstrain describe the electrochemical performance of the examined Li- and Mn-rich CAMs in an almost quantitative manner. Here, the BET surface area represents the CAM/electrolyte interfacial surface area, which dictates the effective charge-transfer resistance of the cathode electrode. This effect can be compensated for by surface normalization of the currents during the discharge rate test (see Fig. 4). On the other hand, the bulk microstrain explains the remaining capacity difference at a given surface-normalized current (see Fig. 8), as it probably controls the lithium diffusion coefficient

and thus determines the extent of the low-voltage redox features below ≈3.6 V. Finally, the post-calcination reveals a strategy to modify these important properties and thus to improve the electrochemical performance of the CAMs.

Conclusions

In this work, we investigated five different Li- and Mn-rich cathode active materials (CAMs), which differ with respect to their morphology (porous vs dense), the incorporation of cobalt (Co-containing vs Co-free), and the secondary agglomerate size (D_{50} values between ≈6 and ≈12 μm). Their initial electrochemical performance is largely different, as evidenced by a discharge rate test, providing capacities from ≈222 mAh g^{-1} down to ≈86 mAh g^{-1} at a practical C-rate of 1C (corresponding to 250 mA g^{-1}). This large variation can be traced back in a quantitative manner to important material metrics, originating both from the surface and from the bulk of the CAMs.

First, the morphology (and to a minor extent the secondary agglomerate size) affects the electrochemically active surface area and thus the effective current density under which the CAMs are operated at a given C-rate. For this reason, the current is referenced to the CAM/electrolyte interfacial surface area, represented here by the BET surface area of the as-received CAMs. In the case of porous CAMs (≈5.3 m^2 g^{-1}), virtually all primary crystallites are exposed to the electrolyte, whereas for dense CAMs (≈0.4–1.3 m^2 g^{-1}) only the outer surface of the secondary agglomerates is in contact with the electrolyte. To account for this difference, the rate test data should be analyzed on the basis of surface-normalized currents (in mA/m^2) rather than on the more commonly used basis of mass-normalized currents (in mA/g). This results in a constant capacity offset among the five investigated CAMs at a given surface-normalized current, revealing that a large fraction (≈50%) of the rate performance differences can be accounted for by their variation in BET surface area. Furthermore, as the internal porosity of the secondary agglomerates cannot easily be removed during the calendaring of the electrodes, the CAM morphology largely affects the electrode density (≈2.2 vs ≈2.7 g$_{electrode}$ cm^{-3}$_{electrode}$ estimated for porous and dense CAMs, respectively) and thus the volumetric energy density of the battery cell.

The remaining capacity differences were shown in turn to scale linearly with the microstrain in the bulk material, which was determined by a size/strain analysis of XPD data. Consequently, the combination of (i) surface normalization of the currents and of (ii) microstrain quantification managed to almost completely capture the achievable capacity of the here examined Li- and Mn-rich layered oxides. The origin of the microstrain remains elusive, because the most common lattice imperfections (viz., in-plane Li/TM ordering and stacking faults, oxygen vacancies, dislocations) could not explain that the capacity contribution of the low-voltage redox feature (below ≈3.6 V vs Li$^+$/Li) substantially decreases with increasing microstrain. The post-calcination of the D-woCo-6 CAM at 1000 °C reduced the microstrain by a factor ≈2.6, thereby also improving its rate capability in comparison to the as-received parent.

This work emphasizes the importance of a proper material characterization, because material metrics such as the specific surface area (from gas physisorption), internal porosity (from Hg intrusion porosimetry), and microstrain (from X-ray powder diffraction) are important performance predictors. They allow for predicting the electrochemical behavior of Li- and Mn-rich CAMs right from their as-received state. Furthermore, we observed no influence of the cobalt content on the performance, i.e., Co can be easily removed from the mixture of Ni-Co-Mn in order to reduce material costs. Attempting to increase the volumetric energy density, however, the replacement of porous CAMs by dense CAMs still must be optimized. The agglomerate size and surface-to-bulk ratio of dense CAMs have to be tuned in such a way that they maintain a reasonable rate capability. Finally, their microstrain in the bulk has to be minimized, which requires the understanding of the underlying lattice imperfection.

Appendix

Electrode density.—The electrode density ($\rho_{electrode}$, in units of g$_{electrode}$/cm^3$_{electrode}$) can be estimated from its individual constituents i and the targeted/achieved electrode porosity (ε^*_{total}) as follows:

$$\rho_{electrode} = (1 - \varepsilon^*_{total}) \cdot \rho_{solids} = (1 - \varepsilon^*_{total}) \cdot \left(\sum_i \frac{\omega_i}{\rho_i} \right)^{-1} \qquad [A\cdot 1]$$

where ω_i is the mass fraction and ρ_i is the crystallographic or particle density of the materials used in the composite electrode. Following the publication by Schreiner et al.,[24] our model electrodes are made of 92.5 wt% CAM (ρ_{CAM} = 4.35 g cm^{-3}), 4.0 wt% C65 conductive carbon (ρ_{C65} = 2.0 g cm^{-3}), and 3.5 wt% PVDF binder (ρ_{PVDF} = 1.76 g cm^{-3}), resulting in an average density of the pure solids of ρ_{solids} = 3.96 g cm^{-3}.

The electrode porosity (ε^*_{total}) is the sum of (i) the inter-particular porosity (ε^*_{inter}) from the pore space between the secondary agglomerates of the CAM as well as the electrode additives, and of (ii) the intra-particular porosity (ε^*_{intra}) between the primary crystallites of the CAM. While ε^*_{inter} can be easily reduced to ≈30% by calendaring, ε^*_{intra} is fairly invariant upon the calendaring process, and thus increases the electrode porosity of an inherently porous CAM.[24] The asterisk (*) indicates that the porosities are based on the electrode level, as opposed to the CAM-based porosity ε_{intra} of the CAM powder that is given in Table I. The conversion of the intra-particular pore volume ($v_{pore,intra}$) obtained from the CAM powder by mercury intrusion porosimetry (see Table I) into the electrode-based intra-particular porosity (ε^*_{intra}) can be done as follows:

$$\varepsilon^*_{intra} = \frac{\omega_{CAM} \cdot v_{pore,intra}}{\omega_{CAM} \cdot v_{pore,intra} + \frac{1}{\rho_{solids}}} \qquad [A\cdot 2]$$

For the above electrode composition, ε^*_{intra} amounts to ≈13.8% for the porous Co-free P-woCo-6 CAM and to ≈2.2% for the dense Co-free D-woCo-6 CAM, respectively. This means that for a typically achieved inter-particular cathode electrode porosity of ε^*_{inter} ≈ 30%, the resulting overall electrode porosity ($\varepsilon^*_{total} = \varepsilon^*_{inter} + \varepsilon^*_{intra}$) would be ≈44% for the porous P-woCo-6 CAM, much higher than that of ≈32% for the dense D-woCo-6 CAM.

Activation cycle.—Figure A·1 shows the voltage profiles of the first activation cycle from the five Li- and Mn-rich layered oxides. As depicted in the inset, there is a substantial spread of the obtained capacities already in the first cycle, whereby the best- and worst-performing CAMs (P-wCo-10 and D-wCo-10) differ by ≈83 mAh g^{-1} during charge and by ≈132 mAh g^{-1} during discharge, respectively. Note that the CAMs are sorted according to their first-cycle discharge capacities in the same order than in the rate test that is following the activation and stabilization cycles (see Fig. 3). The first-cycle Coulombic efficiencies (CEs; see dashed lines) range from close to 90% for the porous CAMs (P-wCo-10 and P-woCo-6) to ≈80% for the D-woCo-6 CAM, all the way down to ≈60% for the dense and Co-containing CAMs (D-wCo-10 and D-wCo-6). For the here examined over-lithiated CAMs with δ = 0.14 ± 0.01, the oxygen release typically starts at a first-cycle charge
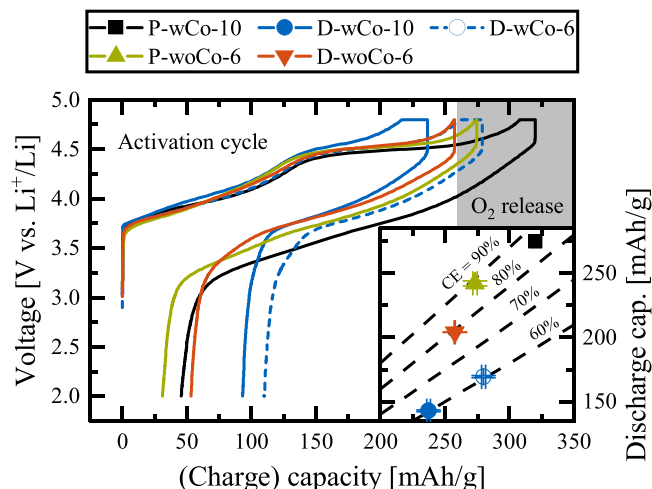
Figure A·1. Activation cycle of the five investigated Li- and Mn-rich layered oxides, which was conducted between 2.0 and 4.8 V vs Li$^+$/Li at a C-rate of either C/10 (with an additional 1 h CV hold at 4.8 V; applied for the Co-containing CAMs) or C/15 (without any CV hold; applied for the Co-free CAMs). Further details can be found in the Experimental section. The gray bar highlights the expected regime for oxygen release.[20,86] The inset shows the first-cycle discharge capacity (right-hand y-axis) as a function of the first-cycle charge capacity; the dashed lines represent different Coulombic efficiencies (CEs).
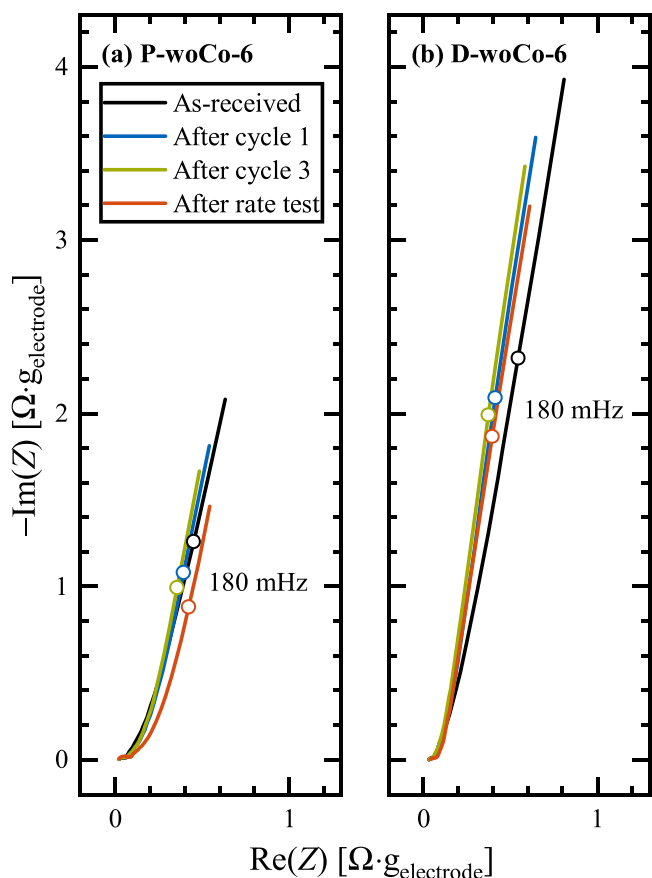

Figure A·3. Specific capacitance of the cathode electrodes over the course of the rate test procedure, as determined from the Nyquist plots in Fig. A·2 (average and min/max values from two cells for each sample). The capacitance of the entire electrode (left y-axis) is converted into the capacitance share of the Co-free CAMs (right y-axis) by subtracting the contribution of the C65 conductive carbon (3.9 F/g$_{C65}$ from a C65 electrode multiplied by its weight fraction of 4 wt% in the actual electrode; see gray bar). The percentages refer to the increase of the CAM capacitance relative to the as-received samples.

capacity of $\approx$260–280 mAh g^{-1} (regime for O$_2$ release highlighted in gray),[20,86] so that we only expect the P-wCo-10 CAM to release lattice oxygen in larger quantities, while minor gas amounts might be evolved from the D-wCo-6 and P-woCo-6 CAMs; however, the D-wCo-10 and D-woCo-6 CAMs should ideally not release any oxygen, at least within the first activation cycle.

Capacitance analysis.—In order to monitor the evolution of the CAM/electrolyte interfacial surface area over the course of the rate test, we used electrochemical impedance spectroscopy (EIS) and applied the capacitance-based method introduced by Oswald et al.[59] For this purpose, we slightly modified the counter-electrode by placing a free-standing graphite (FSG) electrode between the lithium metal foil and the glass-fiber separator, as described by Morasch et al.[87] The impedance contribution of this Li/FSG composite electrode to the WE + CE impedance is negligibly small compared to that of the cathode electrode, so that the cell impedance largely represents the cathode impedance of the Li- and Mn-rich CAM. Electrochemical impedance spectra were measured in blocking conditions (i.e., in the fully discharged state after a constant voltage hold at 2.0 V for 1 h) for the freshly assembled cell, after the activation cycle, after two more stabilization cycles, and at the end of the entire test procedure (with in total 23 cycles). The Nyquist plots of both Co-free CAMs (P-woCo-6 and D-woCo-6) are shown in Fig. A·2. Since the CAMs have a quasi-infinite charge-transfer resistance in their fully discharged (i.e., lithiated) state, the impedance response shows only capacitive behavior, so that the capacitance is a direct measure of the electrode's surface area.[59]

Now, the cathode electrode capacitance can be determined from the imaginary impedance (Im(Z_{f_0})) at the frequency point of $f_0 = $ 180 mHz according to $C \approx 1/(2\pi \cdot f_0 \cdot (-\text{Im}(Z_{f_0})))$. The electrode capacitance (in units of F/g$_{electrode}$) can be converted into the CAM capacitance (in units of F/g$_{CAM}$) originating solely from the Li- and Mn-rich layered oxide by subtracting the capacitance share of the C65 conductive carbon (4.0 wt% C65 and 3.9 F/g$_{C65}$, as determined

Figure A·2. Nyquist plots at selected points before and after the discharge rate test of **(a)** the P-woCo-6 CAM and of **(b)** the D-woCo-6 CAM. After an additional 1 h CV step at the lower cut-off voltage of 2.0 V, the potential-controlled EIS measurements of the modified cells with a Li/FSG counter-electrode were conducted in blocking conditions at 2.0 V and 25 °C with a VMP-300 potentiostat (BioLogic, France) in the frequency range of 100 kHz to 100 mHz and with an AC voltage perturbation of 15 mV. The frequency points at 180 mHz are indicated by empty circles.
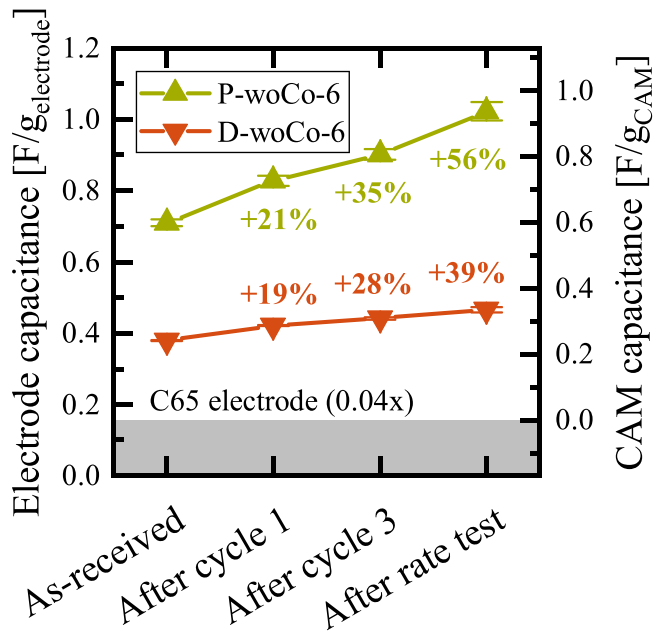
from a C65 electrode (C65:PVDF 50:50 wt%) under the same conditions). The electrode and CAM capacitance of the Co-free materials are plotted in Fig. A·3.

For the as-received samples directly after cell assembly, the CAM capacitance that is proportional to the CAM/electrolyte interfacial surface area amounts to $\approx$0.60 F/g$_{CAM}$ for the porous P-woCo-6 CAM (in green) and to $\approx$0.24 F/g$_{CAM}$ for the dense D-woCo-6 CAM (in red), respectively. Thus, the capacitance ratio of 0.60/0.24 $\approx$ 2.5 is slightly lower than the BET surface area ratio of 5.4/1.3 $\approx$ 4.2 (see Table I), which might be related to the inability of the electrolyte to penetrate into very small pores within the secondary agglomerates of the porous CAM (see Fig. 1d4), in contrast to the penetration by nitrogen during the BET measurement. The extent of capacitance increase, however, is very similar for the porous and dense CAMs, being most pronounced within the first three cycles and amounting to $\approx$40%–60% increase at the end of rate test procedure.

ORCID

Benjamin Strehle https://orcid.org/0000-0001-8878-1160
Franziska Friedrich https://orcid.org/0000-0001-9400-1212
Hubert A. Gasteiger https://orcid.org/0000-0001-8199-8703

References

1. D. Andre, S.-J. Kim, P. Lamp, S. F. Lux, F. Maglia, O. Paschos, and B. Stiaszny, *J. Mater. Chem. A*, **3**, 6709 (2015).
2. R. Schmuch, R. Wagner, G. Hörpel, T. Placke, and M. Winter, *Nat. Energy*, **3**, 267 (2018).
3. Y. Ding, Z. P. Cano, A. Yu, J. Lu, and Z. Chen, *Electrochem. Energy Rev.*, **2**, 1 (2019).
4. P. Rozier and J. M. Tarascon, *J. Electrochem. Soc.*, **162**, A2490 (2015).
5. J. Hong, H. Gwon, S.-K. Jung, K. Ku, and K. Kang, *J. Electrochem. Soc.*, **162**, A2447 (2015).
6. M. M. Thackeray, S.-H. Kang, C. S. Johnson, J. T. Vaughey, R. Benedek, and S. A. Hackney, *J. Mater. Chem.*, **17**, 3112 (2007).
7. Z. Lu, L. Y. Beaulieu, R. A. Donaberger, C. L. Thomas, and J. R. Dahn, *J. Electrochem. Soc.*, **149**, A778 (2002).
8. D.-K. Lee, S.-H. Park, K. Amine, H. J. Bang, J. Parakash, and Y.-K. Sun, *J. Power Sources*, **162**, 1346 (2006).
9. W.-C. Chen, Y.-F. Song, C.-C. Wang, Y. Liu, D. T. Morris, P. A. Pianetta, J. C. Andrews, H.-C. Wu, and N.-L. Wu, *J. Mater. Chem. A*, **1**, 10847 (2013).
10. X. Zhang, X. Meng, J. W. Elam, and I. Belharouak, *Solid State Ionics*, **268**, 231 (2014).
11. E. A. Olivetti, G. Ceder, G. G. Gaustad, and X. Fu, *Joule*, **1**, 229 (2017).
12. C. Banza Lubaba Nkulu et al., *Nat. Sustain.*, **1**, 495 (2018).
13. A. H. Tkaczyk, A. Bartl, A. Amato, V. Lapkovskis, and M. Petranikova, *J. Phys. D: Appl. Phys.*, **51**, 203001 (2018).
14. J. Zheng, S. Myeong, W. Cho, P. Yan, J. Xiao, C. Wang, J. Cho, and J. Zhang, *Adv. Energy Mater.*, **7**, 1601284 (2017).
15. J. R. Croy, K. G. Gallagher, M. Balasubramanian, Z. Chen, Y. Ren, D. Kim, S.-H. Kang, D. W. Dees, and M. M. Thackeray, *J. Phys. Chem. C*, **117**, 6525 (2013).
16. H. Konishi, T. Hirano, D. Takamatsu, A. Gunji, X. Feng, S. Furutsuki, S. Takahashi, and S. Terada, *Solid State Ionics*, **300**, 120 (2017).
17. J. R. Croy, D. Kim, M. Balasubramanian, K. Gallagher, S.-H. Kang, and M. M. Thackeray, *J. Electrochem. Soc.*, **159**, A781 (2012).
18. D. Streich, A. Guéguen, M. Mendez, F. Chesneau, P. Novák, and E. J. Berg, *J. Electrochem. Soc.*, **163**, A964 (2016).
19. B. Strehle, K. Kleiner, R. Jung, F. Chesneau, M. Mendez, H. A. Gasteiger, and M. Piana, *J. Electrochem. Soc.*, **164**, A400 (2017).
20. T. Teufl, B. Strehle, P. Müller, H. A. Gasteiger, and M. A. Mendez, *J. Electrochem. Soc.*, **165**, A2718 (2018).
21. T. Teufl, D. Pritzl, P. Krieg, B. Strehle, M. A. Mendez, and H. A. Gasteiger, *J. Electrochem. Soc.*, **167**, 110505 (2020).
22. S. Hy, H. Liu, M. Zhang, D. Qian, B.-J. Hwang, and Y. S. Meng, *Energy Environ. Sci.*, **9**, 1931 (2016).
23. F. Schipper et al., *Inorganics*, **5**, 32 (2017).
24. D. Schreiner et al., *J. Electrochem. Soc.*, **168**, 030507 (2021).
25. L. Kraft, T. Zünd, D. Schreiner, R. Wilhelm, F. J. Günter, G. Reinhart, H. A. Gasteiger, and A. Jossen, *J. Electrochem. Soc.*, **168**, 020537 (2021).
26. H. Liu et al., *J. Mater. Chem. A*, **6**, 4189 (2018).
27. P. M. Csernica et al., *Nat. Energy*, **6**, 642 (2021).
28. L. Yin et al., *Chem. Mater.*, **32**, 1002 (2020).
29. A. Singer et al., *Nat. Energy*, **3**, 641 (2018).
30. M. Mock, M. Bianchini, F. Fauth, K. Albe, and S. Sicolo, *J. Mater. Chem. A*, **9**, 14928 (2021).
31. S. Ahmed, A. Pokle, M. Bianchini, S. Schweidler, A. Beyer, T. Brezesinski, J. Janek, and K. Volz, *Matter*, **4**, 3953 (2021).
32. S. Ahmed et al., *ACS Nano*, **13**, 10694 (2019).
33. P. Staron et al. (ed.), *Neutrons and Synchrotron Radiation in Engineering Materials Science* (Wiley, Weinheim, Germany) (2017).
34. G. Williamson and W. Hall, *Acta Metall.*, **1**, 22 (1953).
35. K. Kleiner, P. Jakes, S. Scharner, V. Liebau, and H. Ehrenberg, *J. Power Sources*, **317**, 25 (2016).
36. C. R. Fell, D. Qian, K. J. Carroll, M. Chi, J. L. Jones, and Y. S. Meng, *Chem. Mater.*, **25**, 1621 (2013).
37. User Manual, *TOPAS 6 Technical Reference* (Bruker AXS GmbH, Karlsruhe, Germany) (2014).
38. P. W. Stephens, *J. Appl. Crystallogr.*, **32**, 281 (1999).
39. A. O. Kondrakov, A. Schmidt, J. Xu, H. Geßwein, R. Mönig, P. Hartmann, H. Sommer, T. Brezesinski, and J. Janek, *J. Phys. Chem. C*, **121**, 3286 (2017).
40. F. Friedrich, B. Strehle, A. T. S. Freiberg, K. Kleiner, S. J. Day, C. Erk, M. Piana, and H. A. Gasteiger, *J. Electrochem. Soc.*, **166**, A3760 (2019).
41. L. Croguennec, C. Pouillerie, A. N. Mansour, and C. Delmas, *J. Mater. Chem.*, **11**, 131 (2001).
42. K. Kleiner, B. Strehle, A. R. Baker, S. J. Day, C. C. Tang, I. Buchberger, F.-F. Chesneau, H. A. Gasteiger, and M. Piana, *Chem. Mater.*, **30**, 3656 (2018).
43. F. Sigel, B. Schwarz, K. Kleiner, C. Dräger, L. Esmezjan, M. Yavuz, S. Indris, and H. Ehrenberg, *Chem. Mater.*, **32**, 1210 (2020).
44. P. Yan, J. Zheng, M. Gu, J. Xiao, J.-G. Zhang, and C.-M. Wang, *Nat. Commun.*, **8**, 14101 (2017).
45. R. D. Shannon, R. C. Shannon, O. Medenbach, and R. X. Fischer, *J. Phys. Chem. Ref. Data*, **31**, 931 (2002).
46. Gas Sorption System Operating Manual, *ASiQwin Software Version 3.01* (Quantachrome Instruments, Boynton Beach, Florida, FL) (2013).
47. A. Coelho, *TOPAS-Academic Version 6* (Coelho Software, Brisbane, Australia) (2016).
48. D. Mohanty, A. Huq, E. A. Payzant, A. S. Sefat, J. Li, D. P. Abraham, D. L. Wood, and C. Daniel, *Chem. Mater.*, **25**, 4064 (2013).
49. J. Sicklinger, H. Beyer, L. Hartmann, F. Riewald, C. Sedlmeier, and H. A. Gasteiger, *J. Electrochem. Soc.*, **167**, 130507 (2020).
50. W. Mao, G. Ai, Y. Dai, Y. Fu, X. Song, H. Lopez, and V. Battaglia, *J. Electrochem. Soc.*, **163**, A3091 (2016).
51. P.-E. Cabelguen, D. Peralta, M. Cugnet, and P. Maillet, *J. Power Sources*, **346**, 13 (2017).
52. K. Kitada, H. Murayama, K. Fukuda, H. Arai, Y. Uchimoto, Z. Ogumi, and E. Matsubara, *J. Power Sources*, **301**, 11 (2016).
53. L. Froboese, P. Titscher, B. Westphal, W. Haselrieder, and A. Kwade, *Mater. Charact.*, **133**, 102 (2017).
54. H. Giesche, *Part. Part. Syst. Charact.*, **23**, 9 (2006).
55. K. G. Gallagher et al., *J. Electrochem. Soc.*, **163**, A138 (2016).
56. A. Kwade, W. Haselrieder, R. Leithoff, A. Modlinger, F. Dietrich, and K. Droeder, *Nat. Energy*, **3**, 290 (2018).
57. T. Teufl, D. Pritzl, S. Solchenbach, H. A. Gasteiger, and M. A. Mendez, *J. Electrochem. Soc.*, **166**, A1275 (2019).
58. H. Sclar et al., *J. Electrochem. Soc.*, **167**, 110563 (2020).
59. S. Oswald, D. Pritzl, M. Wetjen, and H. A. Gasteiger, *J. Electrochem. Soc.*, **167**, 100511 (2020).
60. J. Liu, H. Chen, J. Xie, Z. Sun, N. Wu, and B. Wu, *J. Power Sources*, **251**, 208 (2014).
61. M. Chouchane, E. N. Primo, and A. A. Franco, *J. Phys. Chem. Lett.*, **11**, 2775 (2020).
62. G. Assat, D. Foix, C. Delacourt, A. Iadecola, R. Dedryvère, and J.-M. Tarascon, *Nat. Commun.*, **8**, 2219 (2017).
63. G. Assat, A. Iadecola, D. Foix, R. Dedryvère, and J.-M. Tarascon, *ACS Energy Lett.*, **3**, 2721 (2018).
64. J. Chen, A. Gutierrez, M. T. Saray, R. S. Yassar, M. Balasubramanian, Y. Wang, and J. R. Croy, *J. Electrochem. Soc.*, **168**, 080506 (2021).
65. A. Gutierrez, J. T. Kirner, M. T. Saray, M. Avdeev, L. Geng, R. S. Yassar, W. Lu, and J. Croy, *J. Electrochem. Soc.*, **169**, 020574 (2022).
66. J. Zheng, W. Shi, M. Gu, J. Xiao, P. Zuo, C. Wang, and J.-G. Zhang, *J. Electrochem. Soc.*, **160**, A2212 (2013).
67. H. Liu, W. Xiang, C. Bai, L. Qiu, C. Wu, G. Wang, Y. Liu, Y. Song, Z.-G. Wu, and X. Guo, *Ind. Eng. Chem. Res.*, **59**, 19312 (2020).
68. P. Vanaphuti, Y. Liu, X. Ma, J. Fu, Y. Lin, J. Wen, Z. Yang, and Y. Wang, *ACS Appl. Mater. Interfaces*, **13**, 22597 (2021).
69. A. Nickol, T. Schied, C. Heubner, M. Schneider, A. Michaelis, M. Bobeth, and G. Cuniberti, *J. Electrochem. Soc.*, **167**, 090546 (2020).
70. N. Yabuuchi, K. Yoshii, S.-T. Myung, I. Nakai, and S. Komaba, *J. Am. Chem. Soc.*, **133**, 4404 (2011).
71. W. E. Gent et al., *Nat. Commun.*, **8**, 2091 (2017).
72. H. Koga, L. Croguennec, P. Mannessiez, M. Ménétrier, F. Weill, L. Bourgeois, M. Duttine, E. Suard, and C. Delmas, *J. Phys. Chem. C*, **116**, 13497 (2012).
73. J. Liu, L. Yin, L. Wu, J. Bai, S.-M. Bak, X. Yu, Y. Zhu, X.-Q. Yang, and P. G. Khalifah, *Inorg. Chem.*, **55**, 8478 (2016).
74. R. Robert, C. Bünzli, E. J. Berg, and P. Novák, *Chem. Mater.*, **27**, 526 (2015).
75. A. Grenier, H. Liu, K. M. Wiaderek, Z. W. Lebens-Higgins, O. J. Borkiewicz, L. F. J. Piper, P. J. Chupas, and K. W. Chapman, *Chem. Mater.*, **29**, 7345 (2017).
76. R. E. Dinnebier, A. Leineweber, and J. S. O. Evans, *Rietveld Refinement: Practical Powder Diffraction Pattern Analysis Using TOPAS* (Walter de Gruyter GmbH, Berlin) (2019).
77. W. E. Gent et al., *Adv. Mater.*, **28**, 6631 (2016).
78. J. Bréger, M. Jiang, N. Dupré, Y. S. Meng, Y. Shao-Horn, G. Ceder, and C. P. Grey, *J. Solid State Chem.*, **178**, 2575 (2005).

79. J. Serrano-Sevillano, D. Carlier, A. Saracibar, J. M. Lopez del Amo, and M. Casas-Cabanas, *Inorg. Chem.*, **58**, 8347 (2019).
80. B. Qiu et al., *Nat. Commun.*, **7**, 12108 (2016).
81. Q. Li et al., *J. Mater. Chem. A*, **8**, 7733 (2020).
82. T. Nakamura, H. Gao, K. Ohta, Y. Kimura, Y. Tamenori, K. Nitta, T. Ina, M. Oishi, and K. Amezawa, *J. Mater. Chem. A*, **7**, 5009 (2019).
83. T. Nakamura, K. Ohta, Y. Kimura, K. Tsuruta, Y. Tamenori, R. Aso, H. Yoshida, and K. Amezawa, *ACS Appl. Energy Mater.*, **3**, 9703 (2020).
84. H. Deng, I. Belharouak, Y.-K. Sun, and K. Amine, *J. Mater. Chem.*, **19**, 4510 (2009).
85. S. Ahmed, M. Bianchini, A. Pokle, M. S. Munde, P. Hartmann, T. Brezesinski, A. Beyer, J. Janek, and K. Volz, *Adv. Energy Mater.*, **10**, 2001026 (2020).
86. T. Zünd, B. Strehle, and H. A. Gasteiger, *ECS Meet. Abstr.*, **MA2019-01**, 510 (2019).
87. R. Morasch, B. Suthar, and H. A. Gasteiger, *J. Electrochem. Soc.*, **167**, 100540 (2020).